2010

Quantifying Vertical Axis Rotation in Curved Orogens: Correlating Multiple Data Sets with a Refined Weighted Least Squares Strike Test

Adolph Yonkee

Arlo Brandon Weil
Bryn Mawr College, aweil@brynmawr.edu

Custom Citation

Yonkee, A., and A. B. Weil (2010) Quantifying vertical axis rotation in curved orogens: Correlating multiple data sets with a refined weighted least squares strike test, *Tectonics*, 29, TC3012.

Quantifying vertical axis rotation in curved orogens: Correlating multiple data sets with a refined weighted least squares strike test

Adolph Yonkee[1] and Arlo Brandon Weil[2]

Received 15 April 2008; revised 10 April 2009; accepted 4 January 2010; published 26 June 2010.

[1] Map-scale curvature is a fundamental feature of most contractional orogenic belts and is central to understanding the kinematic and dynamic evolution of mountain systems. Paleomagnetic analysis, combined with detailed structural studies, is the most robust means of quantifying vertical axis rotations that produce curvature over a range of temporal and spatial scales. This paper explores how vertical axis rotations can best be evaluated for multiple data sets by applying a weighted least squares method to the classic strike test. This refined method provides measures of best fit slope, confidence interval, and goodness of fit between map-scale structural trend, paleomagnetic rotations, and deformation fabric orientations. Structural trend is estimated by averaging fold axial trace, formation contact, and bed strike data over kilometer-scale areas. Paleomagnetic and deformation fabric site-mean orientations and measurement uncertainties are estimated using vector and bootstrap statistics. Weighting factors are estimated from combined measurement uncertainty, structural noise related to small-scale block rotation and stress/strain refraction, and variations in restoration paths. The number of sites needed to obtain a significant confidence interval in strike test slope is a function of combined uncertainty in paleomagnetic or deformation fabric directions and the total range in structural trend around a curved orogen. Improved estimates of strike test slope and rotation thus require systematic sampling with a wide distribution of sites, evaluation of appropriate weighting factors, and statistical analysis. A case study is presented that highlights application of this refined method to paleomagnetic and deformation fabric data sets from the Wyoming salient of the Sevier thrust belt. Paleomagnetic data yield a strike test slope of 0.76 ± 0.11, indicating that the Wyoming salient is a progressive arc, with ~3/4 secondary curvature related to vertical axis rotation synchronous with large-scale thrusting and ~1/4 initial curvature. Finite strain, anisotropy of magnetic susceptibility, and mesoscopic structural orientations, which are related to early layer-parallel shortening, all yield strike test slopes of ~0.9 ± 0.1. Comparing these slopes with paleomagnetic results indicates that deformation fabrics had initial curvature and thus cannot be used alone to accurately estimate rotations. By integrating systematic paleomagnetic and structural data using statistical analysis, curvature models for the Wyoming salient are closely constrained. **Citation:** Yonkee, A., and A. B. Weil (2010), Quantifying vertical axis rotation in curved orogens: Correlating multiple data sets with a refined weighted least squares strike test, *Tectonics*, *29*, TC3012, doi:10.1029/2008TC002312.

1. Introduction

[2] Accurately quantifying vertical axis rotation over a range of temporal and spatial scales is critical for understanding processes that produce curved mountain systems [e.g., *Sussman and Weil*, 2004; *Van der Voo*, 2004; *Marshak*, 2004]. Curved orogenic belts can be broadly divided into primary arcs, progressive arcs, and secondary oroclines, based on timing relations between deformation and curvature [*Weil and Sussman*, 2004]. Primary arcs begin with curvature and do not experience additional rotation, progressive arcs develop increasing structural curvature and vertical axis rotation during deformation, and secondary oroclines experience rotation of an original linear belt during a subsequent phase of deformation (Figure 1). Traditionally, the best way to quantify vertical axis rotation has been through paleomagnetic analysis [e.g., *Irving and Opdyke*, 1965; *Kotasek and Krs*, 1965; *Grubbs and Van der Voo*, 1976; *Channell et al.*, 1978; *Van der Voo and Channell*, 1980; *Schwartz and Van der Voo*, 1984; *Kent and Opdyke*, 1985; *Eldredge et al.*, 1985; *Lowrie and Hirt*, 1986; *Miller and Kent*, 1986a, 1986b; *Eldredge and Van der Voo*, 1988; *Kent*, 1988; *Muttoni et al.*, 1998, 2000; *Weil et al.*, 2000, 2001; *Weil*, 2006]. Such analysis, if carefully done at appropriate scales, can track magnitudes of block rotations between individual sites and provide key data to test various kinematic models. Vertical axis rotation, however, is just one component of the full three-dimensional deformation field, and thus any viable kinematic model must also be consistent with other structural data. Layer-parallel shortening (LPS) fabrics that form early in the deformation history are widespread in many orogenic belts, and provide additional constraints for kinematic models [e.g., *Geiser and Engelder*, 1983; *Mitra*, 1994; *Gray and Stamatakos*, 1997; *Hogan and Dunne*, 2001; *Ong et al.*, 2007]. Tangential extension or shortening parallel to structural trend may also be an important component of deformation [*Ries and*

[1]Department of Geosciences, Weber State University, Ogden, Utah, USA.
[2]Department of Geology, Bryn Mawr College, Bryn Mawr, Pennsylvania, USA.

0278-7407/10/2008TC002312

Shackleton, 1976; *Ferrill and Groshong*, 1993; *Marshak*, 2004]. Consequently, to develop robust kinematic models for orogenic curvature, one needs to analyze multiple data sets, evaluate uncertainties in data, and estimate confidence intervals for fitted model parameters. Ultimately, such kinematic models provide important information about mechanical processes responsible for evolution of curved mountain systems, including critical wedge dynamics.

[3] Although components of vertical axis rotation have been evaluated from paleomagnetic and structural studies in multiple orogenic belts, different studies have interpreted different rotation patterns, both within and between different belts. For example, previous studies in the Alps have yielded

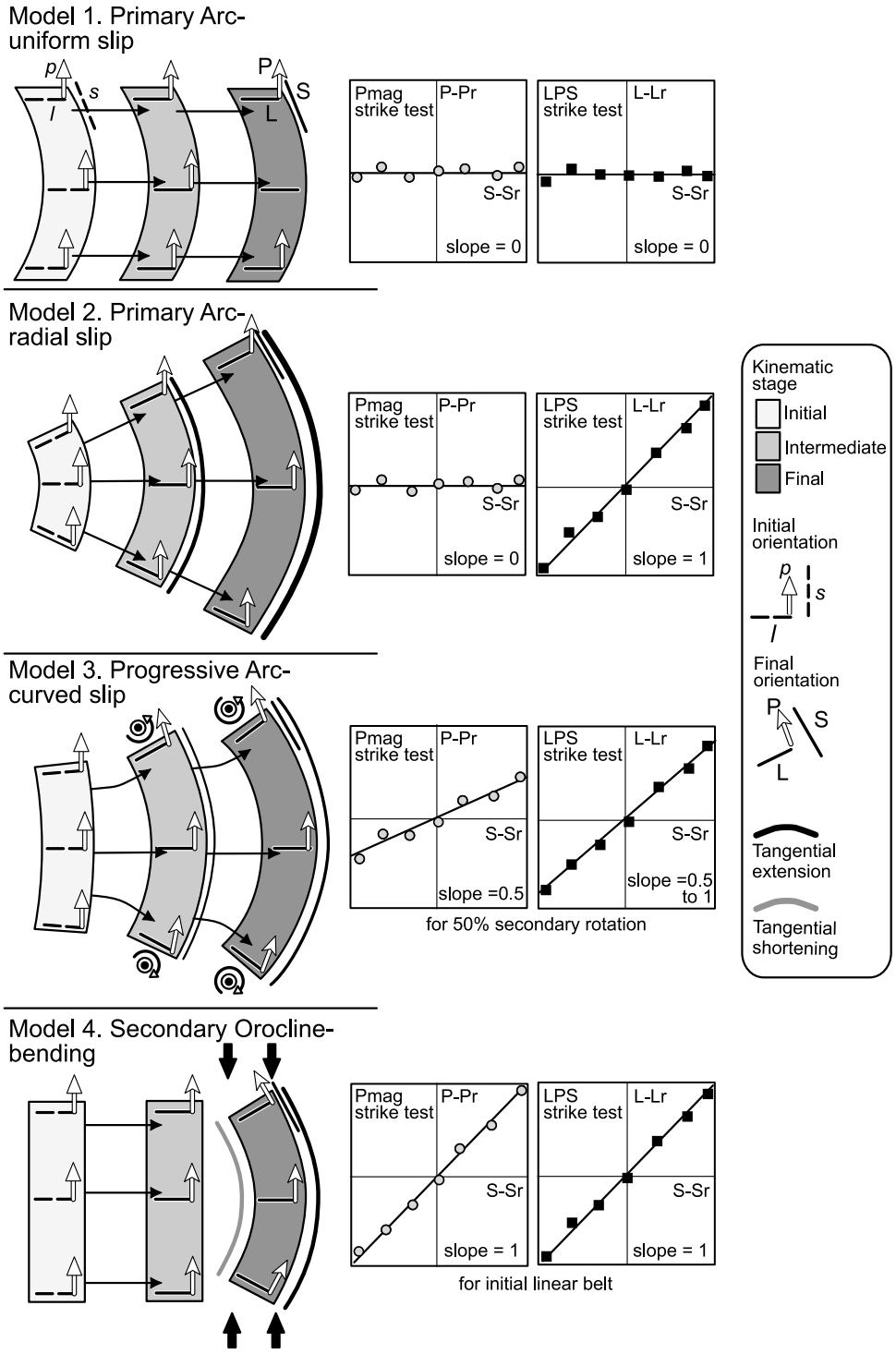

Figure 1

various interpretations, including: (1) a primary arc with no significant vertical axis rotation [*Lowrie and Hirt*, 1986; *Hirt and Lowrie*, 1988]; (2) a progressive arc with rotation concentrated at the advancing orogenic front [*Hindle and Burkhard*, 1999]; (3) superimposed oroclinal bending of an originally linear orogen [*Channell et al.*, 1978; *Eldredge et al.*, 1985; *Muttoni et al.*, 1998, 2000]; and (4) multiple episodes of deformation with different shortening directions that produced intersecting structural trends [*Lickorish et al.*, 2002]. Previous workers in the Appalachian orogen have also arrived at multiple interpretations, from a primary arc [*Schwartz and Van der Voo*, 1983; *Eldredge et al.*, 1985; *Stamatakos and Hirt*, 1994; *Cederquist et al.*, 2006], to varying components of localized and regional secondary rotation [*Kent and Opdyke*, 1985; *Kent*, 1988; *Miller and Kent*, 1986a, 1986b; *Gray and Stamatakos*, 1997; *Ong et al.*, 2007]. Early paleomagnetic studies in the Cantabrian-Asturian Arc, northern Spain, argued for partial secondary curvature [*Perroud*, 1986; *Hirt et al.*, 1992; *Parés et al.*, 1994; *Stewart*, 1995; *Van der Voo et al.*, 1997] but were hampered by limited sampling and incomplete understanding of secondary remagnetization components. Recently, *Weil et al.* [2000, 2001] and *Weil* [2006] showed that remagnetization patterns are consistent with secondary oroclinal bending of an originally linear belt. These examples illustrate the difficulties in quantifying rotation patterns, which are partly related to limited sampling, structural complexities, multiple remagnetizations, and incomplete statistical analysis.

[4] This paper explores how vertical axis rotations can best be evaluated at a regional scale using multiple data sets. The following questions will be addressed using a refined statistical approach to the classic strike test:

[5] 1. What is the best method to obtain estimates of rotation and uncertainties?

[6] 2. What is an appropriate sampling design?

[7] 3. What is the best way to integrate and compare multiple data sets?

[8] A case study is presented that highlights application of this approach to paleomagnetic and deformation fabric data sets from the Wyoming salient of the Sevier thrust belt.

2. Strike Test Methodology

2.1. Overview

[9] Correlations between changes in regional structural trend (relative to a reference trend for an orogen), and rotations estimated from paleomagnetic or deformation fabric directions (relative to a reference direction) can be evaluated using a strike test, also called an orocline test [*Schwartz and Van der Voo*, 1983; *Eldredge et al.*, 1985; *Lowrie and Hirt*, 1986]. Four simple end-member kinematic models are shown in Figure 1. For model 1 (primary arc with uniform thrust slip), both paleomagnetic and LPS directions remain unchanged, and both strike tests have a slope of 0. All curvature is primary, with constantly oriented LPS directions. For model 2 (primary arc with radial slip), paleomagnetic directions are not rotated and define a slope of 0, whereas radial LPS directions define a slope of 1. All curvature is primary, but with initial radial LPS fabrics that undergo spreading. For model 3 (progressive arc with curved thrust slip), both paleomagnetic and LPS directions progressively rotate with changes in structural trend, and strike tests for both data sets have slopes between 0 and 1, depending on the amount of curvature present when magnetizations and LPS fabrics develop. For model 4 (secondary orocline with superimposed bending), a belt with initially linear thrusts and consistent LPS fabrics undergoes 100% secondary rotation during a subsequent deformation phase, yielding slopes of 1 for both paleomagnetic and LPS directions. In summary, a strike test slope of 0 for paleomagnetic data indicates a primary arc, an intermediate slope indicates a progressive arc (with the slope giving the percentage of secondary curvature acquired subsequent to magnetization), and a slope of 1 indicates a secondary orocline. A strike test slope for deformation fabric data, however, can only be uniquely interpreted if constraints can be placed on initial fabric orientation.

[10] In detail, individual site paleomagnetic and deformation fabric directions may depart from ideal relations due to measurement uncertainties, structural noise, and complex deformation paths (Figure 2). Additionally, nonlinear relations between paleomagnetic directions and structural trend may occur if secondary rotation is highly concentrated, such as within transfer zones. Thus, a method is needed to estimate best fit models, evaluate uncertainties in input data and fitted parameters, and integrate multiple data sets.

2.2. Statistical Methods

[11] Correlations between regional structural trend (x), and either paleomagnetic or deformation fabric directions (y) relative to a reference direction can be quantified using a weighted least squares method. This method provides the maximum likelihood estimate of strike test slope if mea-

Figure 1. (left) Idealized end-member kinematic models for curved orogenic belts. Initial/final paleomagnetic declinations (p/P), layer-parallel shortening directions (l/L), structural trends (s/S), tangential strains (line width proportional to magnitude), and displacement paths indicated for initial, intermediate, and final stages of deformation. (right) Corresponding strike test plots illustrate relations between paleomagnetic declinations relative to reference declination (P-Pr), layer-parallel shortening (LPS) direction relative to reference (L-Lr), and structural trend relative to reference (S-Sr). For model 1 (primary arc with uniform slip) both paleomagnetic and LPS directions define slopes of 0. For model 2 (primary arc with radial slip) the paleomagnetic slope is 0, whereas the LPS slope is 1. For model 3 (progressive arc with curved slip) the paleomagnetic slope gives the component of secondary rotation since magnetization, and the LPS slope lies between the paleomagnetic slope and 1, depending on the amount of initial curvature in LPS directions. For model 4 (secondary orocline with bending of a linear belt) both paleomagnetic and LPS directions define a slope of 1. Individual site values may depart from the best fit slope due to uncertainties in site directions.

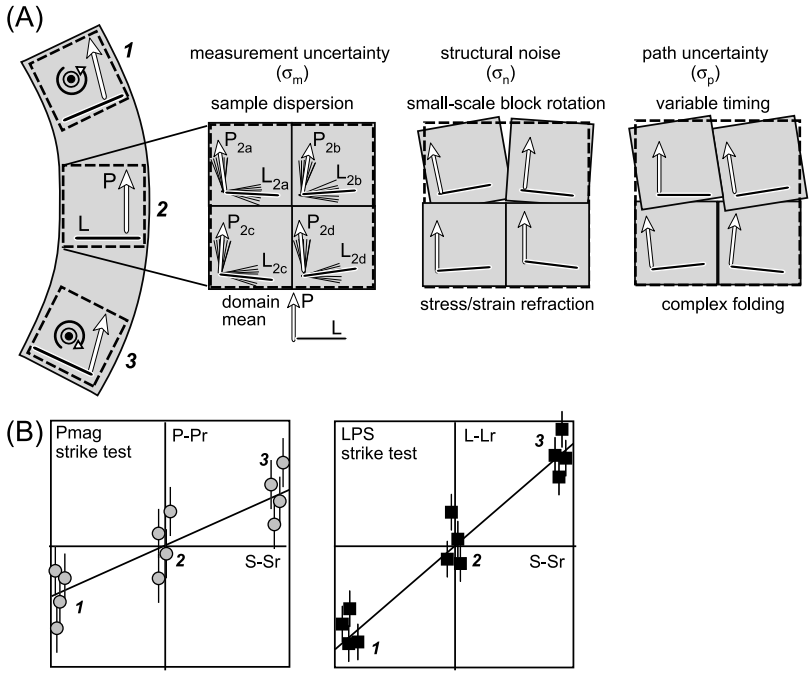

Figure 2. Relations between uncertainties in site directions and strike tests. (a) (left) Idealized model for a progressive arc with paleomagnetic declinations (P, arrows) and LPS directions (L, bold lines) shown for three domains. (right) Schematic diagrams show four local blocks/sites in the central domain with measurement uncertainty (σ_m) from dispersion of individual paleomagnetic and LPS sample data (indicated by short lines) about site means, which in turn vary about the regional mean; structural noise (σ_n) related to small-scale block rotations and stress/strain refraction; and path uncertainty (σ_p) related to variable timing relations and complex folding with different restorations leading to apparent (spurious) rotations. (b) Corresponding strike tests for paleomagnetic and LPS data. Individual site-mean directions for each domain are normally distributed about the best fit line, with error bars that reflect total uncertainty, given by $\sigma_y^2 = \sigma_m^2 + \sigma_n^2 + \sigma_p^2$.

surement errors are independent and normally distributed. For a linear model and the case where uncertainty in x is small, the best fit slope, m, and intercept, b, are obtained by minimizing the total weighted misfit, χ^2, given by

$$\chi^2 = \sum_{j=1,N}\left[(y_j - mx_j - b)^2\omega_j\right] = \sum_{j=1,N}(e_j)^2\omega_j \qquad \omega_j = 1/\sigma_{yj}^2 \tag{1}$$

where N is the number of sites, e_j is the residual for the jth site, and ω_j and σ_{yj} are the weighting factor and uncertainty for the jth site direction. The best fit slope, intercept, and standard errors in estimates, δ_m and δ_b, are given by

$$m = (S * S_{xy} - S_x * S_y)/\Delta \qquad b = \bar{y} - m\bar{x} \qquad \delta_m = \sqrt{S/\Delta} \qquad \delta_b = \sqrt{S_{xx}/\Delta} \tag{2}$$

where

$$S = \sum_{j=1,N}(\omega_j); S_x = \sum_{j=1,N}(x_j\omega_j); S_y = \sum_{j=1,N}(y_j\omega_j);$$
$$\bar{x} = S_x/S; \bar{y} = S_y/S$$
$$S_{xx} = \sum_{j=1,N}(x_jx_j\omega_j); S_{xy} = \sum_{j=1,N}(x_jy_j\omega_j); \Delta = S*S_{xx} - S_x*S_x$$

The corresponding 95% confidence interval in slope is $\pm 1.96*\delta_m$. If the intercept is statistically insignificant ($|b| < 1.96*\delta_b$), then equation (1) can be recast with $b = 0$ and minimized with respect to m, giving $m = S_{xy}/S_{xx}$. Note, changing the reference direction for paleomagnetic or deformation fabric data only changes the intercept but does not change m and δ_m. Goodness of fit (i.e., acceptability of the model) is given by

$$Q = \Gamma[(N-2)/2, \chi^2/2] \tag{3}$$

where Γ is the incomplete gamma function for $N-2$ degrees of freedom and χ^2 misfit, and Q is the probability the weighted misfit could be produced by the model; a value of $Q \geq 0.1$ is generally considered acceptable [*Bevington*, 1969]. For a given N, Q decreases as χ^2 increases, related

to increasing site residuals, e_j, or decreasing site uncertainties, σ_{yj}. Note, if site uncertainties are incorrectly set too small, then confidence intervals will appear to decrease, but χ^2 will increase and goodness of fit will be unacceptably low ($Q < 0.1$). Additionally, residuals should be approximately normally distributed and uncorrelated for an acceptable model.

[12] For the general case of uncertainty in both x and y (with no correlation between measurement errors), the best fit slope and intercept are obtained by minimizing

$$\chi^2 = \sum_{j=1,N}\left[(y_j - mx_j - b)^2\omega_j\right]$$
$$\omega_j = 1/(\sigma_{yj}^2 + m^2\sigma_{xj}^2) \quad (4)$$

where the weighting factor reflects uncertainties σ_{yj} and σ_{xj} in both y_j and x_j [*York*, 1968]. The best fit slope, intercept, and standard errors for this case are given by

$$m = (S_{xy}* - S_{yy}*)/(S_{xx}* - S_{yx}*)$$
$$b = \bar{y} - m\bar{x}$$
$$\delta_m = \sqrt{1/S_{xx}} \quad (5)$$
$$\delta_b = \delta_m\sqrt{S_{xx}/S}$$

where

$$S_{xy}* = \sum_{j=1,N}(x_j - x_m)*(y_j - y_m)\omega_j^2\sigma_{yj}^2;$$
$$S_{yy}* = \sum_{j=1,N}(y_j - y_m)^2\omega_j^2(m\sigma_{xj})^2$$
$$S_{xx}* = \sum_{j=1,N}(x_j - x_m)\omega_j^2\sigma_{yj}^2;$$
$$S_{yx}* = \sum_{j=1,N}(y_j - y_m)*(x_j - x_m)\omega_j^2(m\sigma_{xj})^2$$

[13] For this case, weighting factors depend on slope, and equations (4) and (5) must be iteratively solved. Note, equation (4) reduces to the simpler case in equation (1) for small σ_{xj}.

[14] Previous studies of orogenic curvature have typically calculated strike test slope with an unweighted least squares method and used the square of the correlation coefficient, R^2, given by

$$R^2 = \left\{\sum_{j=1,N}\left[(y_j - y_m)(x_j - x_m)\right]\right\}^2 \Big/ \cdot\left\{\left[\sum_{j=1,N}(y_j - y_m)^2\right]\left[\sum_{j=1,N}(x_j - x_m)^2\right]\right\} \quad (6)$$

to interpret 'fit'. This measure, although giving a general indication of correlation strength, does not provide quantitative estimates of confidence intervals, nor a measure of acceptability of the model. Thus, an unweighted method not only gives equal consideration to both poorly and precisely constrained data points, but also does not provide confidence intervals needed to test statistical significance of slopes.

2.3. Scale and Sampling Design

[15] Strike tests are designed to test systematic correlation between regional curvature and rotations. However, random noise may be present and scale must be considered in sampling design. Typically, regional structural trend is evaluated from map patterns at scales on the order of kilometers, whereas site data are collected from outcrops at scales on the order of meters. Sites should be chosen from outcrops that display consistent bedding and deformation fabric orientations. Individual site directions, however, may still vary due to measurement uncertainty, structural noise, and complex deformation paths (Figure 2). Site locations should be chosen to optimize along-strike coverage, with local sampling arrays designed to check for potential complications. This is exemplified by considering a simple case with $N + 1$ sites distributed at equal trend increments of $\Delta x/N$ over a total range in trend of Δx, and with constant site uncertainty in paleomagnetic or deformation fabric directions, σ_y. For this case, the standard error in slope is given by (for large N)

$$\delta_m \approx 3.5\sigma_y\sqrt{1/N}(1/\Delta x) \quad (7)$$

[16] Thus, the slope error (and 95% confidence interval = $\pm 1.96*\delta_m$) can be improved by decreasing site uncertainty, increasing the total number of sites, and increasing the range in trend (Figure 3). Note, the confidence interval does not depend on slope. In contrast, the correlation coefficient, R, depends on slope but does not depend on site uncertainty nor on the number of sites (except at low N), and therefore is a poor measure of fit (Figure 3). Recasting equation (7) as

$$N \approx 12 * \sigma_y^2/(\delta_m\Delta x)^2 \quad (8)$$

gives an approximation for the number of sites needed to give a desired confidence interval, $\pm c*\delta_m$. For example, to obtain a 95% confidence interval of ±0.1 (c = 1.96, δ_m =

Figure 3. Monte Carlo simulations of strike tests for four cases (A to D) with different numbers of sites (N), total change in structural trend (Δx), and input slope (m); site direction uncertainty is constant ($\sigma_y = 10°$). Two examples of data point simulations, best fit slope (m*), standard error for simulation (δ*), and square of correlation coefficient (R^2*) are shown for each case. Dashed line represents 1σ spread about the input slope (i.e., ~70% of simulated points should lie between dashed lines). Histograms show best fit slopes and R^2* values from 1000 simulations for each case, with mean values listed. For each case, best fit slopes display a normal distribution, with a mean equal to the input slope and a standard deviation (s_{m*}) equal to the standard error (δ). The standard error (and 95% confidence interval is 1.96δ) increases as N decreases (compare cases A and B), increases as Δx decreases (compare cases A and C), and does not depend on slope (compare cases A and D). In contrast, R^2* values for simulations do not have normal distributions, are insensitive to N (compare cases A and B), and depend on slope (compare cases A and D).

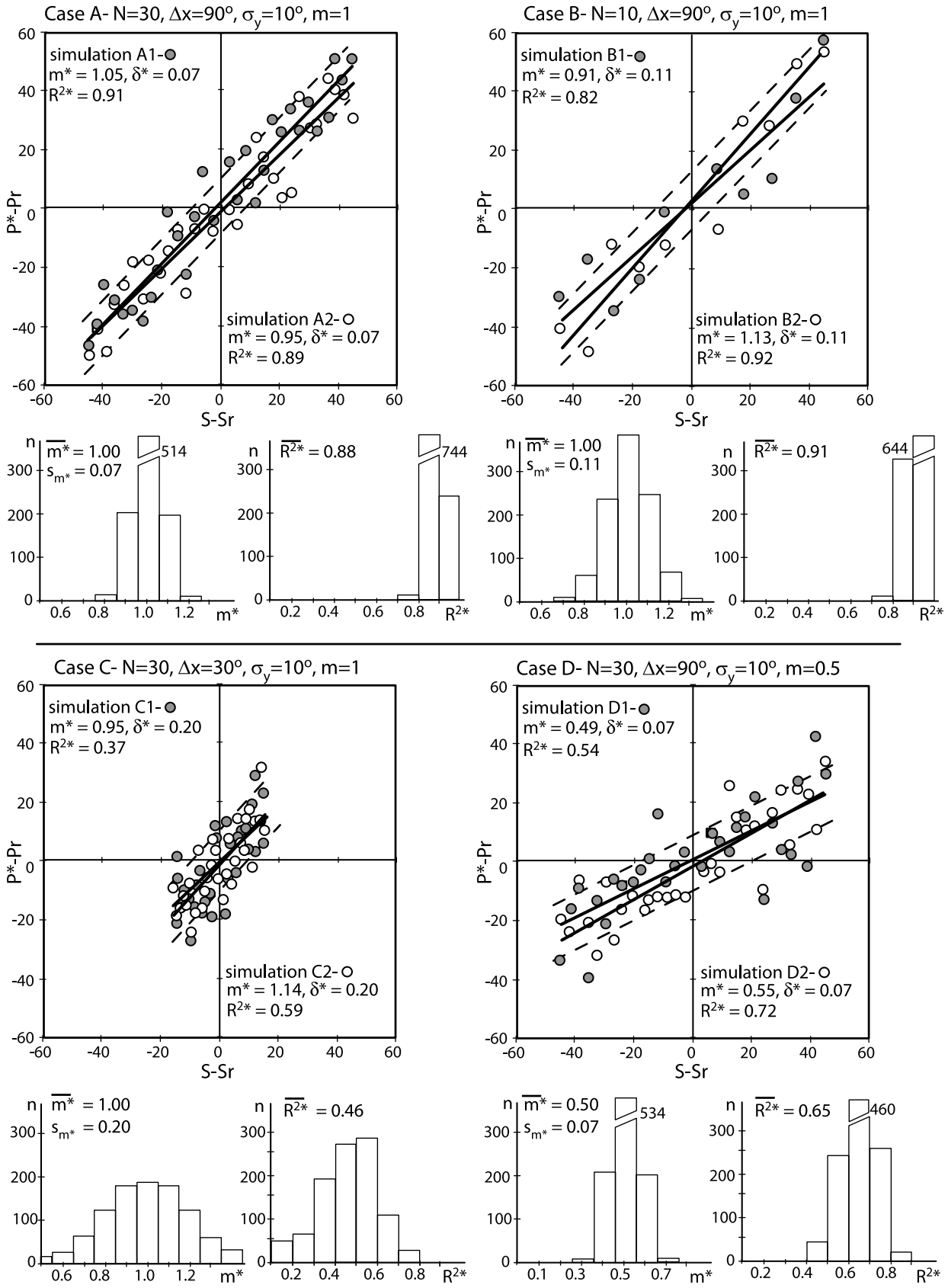
Case A- N=30, Δx=90°, σy=10°, m=1
simulation A1-
m* = 1.05, δ* = 0.07
R2* = 0.91
simulation A2-
m* = 0.95, δ* = 0.07
R2* = 0.89
P*-Pr
S-Sr
m* = 1.00
sm* = 0.07
514
R2* = 0.88
744
Case B- N=10, Δx=90°, σy=10°, m=1
simulation B1-
m* = 0.91, δ* = 0.11
R2* = 0.82
simulation B2-
m* = 1.13, δ* = 0.11
R2* = 0.92
m* = 1.00
sm* = 0.11
R2* = 0.91
644
Case C- N=30, Δx=30°, σy=10°, m=1
simulation C1-
m* = 0.95, δ* = 0.20
R2* = 0.37
simulation C2-
m* = 1.14, δ* = 0.20
R2* = 0.59
m* = 1.00
sm* = 0.20
R2* = 0.46
Case D- N=30, Δx=90°, σy=10°, m=0.5
simulation D1-
m* = 0.49, δ* = 0.07
R2* = 0.54
simulation D2-
m* = 0.55, δ* = 0.07
R2* = 0.72
m* = 0.50
sm* = 0.07
534
R2* = 0.65
460
n
m*
R2*

Figure 3

0.05), $N = 60$ sites are needed for a total range in structural trend of $\Delta x = 90°$ and $\sigma_y = 10°$. More sites are needed if Δx is smaller or site uncertainty is greater. Although relations are more complex for unequally spaced sites, the same general conclusions apply.

2.4. Evaluation of Structural Trend

[17] Structural trend for a site, x_j, is best estimated from geologic map patterns compiled from kilometer-scale areas to average out local noise, being careful to account for topographic effects and fold plunge. Fold axial traces, formation contacts, and bedding strikes along fold limbs or within dip panels above frontal thrust ramps are all useful for estimating regional structural trend. Thrust traces and formation contacts in areas of low dip are strongly influenced by topography and subsequent tilting, and thus should be used with caution. Analysis of bedding and fold trace data for a detailed study area in the Wyoming salient illustrates how structural trend and uncertainty can be evaluated. In the example area, individual bedding strikes (corrected for fold plunge) display dispersion about the mean trend, with a standard deviation of $s_t = 14°$ (in detail dispersion varies with bed dip) (Figure 4b). Dispersion reflects minor warping oblique to regional trend, tilting over oblique minor faults, and local block rotation. Failure to correct for fold plunge increases strike dispersion and introduces bias on fold limbs. Despite dispersion of individual strike values, the mean structural trend for the area is well constrained due to a large number of readings ($n = 74$), with an uncertainty of $\sigma_x \approx s_t/\sqrt{n} = 2°$. If uncertainty in regional trend is small when averaged over a large area, then equations (1) and (2) can be used to calculate strike test slope and confidence intervals. If bed strike measured at a single site is used, then contributions from local noise should be included ($\sigma_x = s_t \sim 10$–$20°$) and equations (4) and (5) used to calculate strike test slope and confidence intervals. Sites located along oblique thrust ramps or transfer zones may have anomalous trends that require separate analysis.

2.5. Evaluation of Paleomagnetic and Deformation Fabric Data

[18] Paleomagnetic declination for a site, y_j, is typically obtained from the vector mean of stable remanent components measured in cores collected from multiple beds in order to average out secular variation. Deformation fabric directions for a site can be estimated using a variety of methods, including finite strain analysis, measurement of anisotropy of magnetic susceptibility (AMS), and orientation analysis of mesoscopic structures, such as cleavage. Finite strain analysis provides a direct measure of principal fabric directions, but markers may not be present everywhere and directions tend to be poorly defined in areas with low strain intensity. AMS measures magnetic mineral fabrics and may provide a proxy for strain directions, but AMS typically records a composite of sedimentary and deformation fabrics (see reviews by *Borradaile and Tarling* [1981], *Rochette et al.* [1992], and *Borradaile and Henry* [1997]). Mesoscopic structures provide another proxy for strain directions, but structures may be modified by shear and form during complex deformation histories. Thus, relations between finite strain, AMS, and mesoscopic structures should be checked for consistency.

[19] Total uncertainty in a paleomagnetic or deformation fabric direction, σ_{yj}, is given by:

$$\sigma_{yj}^2 = \sigma_m^2 + \sigma_n^2 + \sigma_p^2 \tag{9}$$

where σ_m is measurement uncertainty in site-mean direction (which typically scales as $\sigma_m \approx s/\sqrt{n}$, where s is sample dispersion and n is number of sample measurements at a site), σ_n is structural noise related to small-scale block rotations and stress/strain refraction between sites, and σ_p is uncertainty from varying restoration paths (Figure 2).

[20] Uncertainty in site-mean paleomagnetic declination, σ_m, is commonly estimated from dispersion of individual core measurements using spherical statistics [*Fisher*, 1953; *Kent*, 1982]. Dispersion reflects secular variation and measurement errors (associated with orienting cores and picking stable remnant components, such as from stepwise thermal demagnetization plots [*Tauxe*, 1998]). Measuring 6 to 10 cores per site typically gives α_{95} cones of ~10 to 15°. Sites with greater dispersion may have additional complications and are generally not used for analysis. Sites with lower dispersion may reflect inadequate sampling to represent secular variation, and should be used cautiously with artificially low α_{95} values adjusted to match expected secular variation [*McFadden et al.*, 1991]. Note, a strike test only compares changes in declination within spherical distributions, yielding the approximate relation $\sigma_m \approx 0.4*\alpha_{95}/\cos(i)$, where i is inclination [*Demarest*, 1983]; this relation breaks down for steep inclinations ($i > 60°$). If multiple magnetic components are present, effects of overprinting should be evaluated, and in deformed areas care is needed to check for modification of remanent directions by strain [*van der Pluijm*, 1987; *Kodama*, 1988; *Stamatakos and Kodama*, 1991a, 1991b; *Borradaile*, 1997].

[21] Uncertainty in finite strain directions can be evaluated using bootstrap resampling or tensor statistics [*McNaught*, 1994; *Mulchrone et al.*, 2003; *Yonkee*, 2005]. For example, uncertainty in 2-D directions determined with the $Rf - \phi$ method is $\sigma_m \approx 30°*[\ln(RI)/\ln(RS)]/\sqrt{n}$, where RI is the initial ratio of markers, RS is the strain ratio, and n is the number of strain markers. For moderate strain ($RS \sim 1.4$) and markers that start close to circular (e.g., reduction spots along bedding planes with $RI \sim 1.1$), measuring ~10 markers gives small uncertainties, whereas for markers that depart from circularity (e.g., angular quartz grains with $RI \sim 1.4$), ~100 grains must be measured to give small uncertainties. Directions tend to be poorly constrained at low strain ($RS < 1.1$). Effects of primary fabrics should also be evaluated [*Paterson et al.*, 1995].

[22] Uncertainty in site AMS directions can be evaluated using parametric bootstrap of individual core measurements [*Constable and Tauxe*, 1990]. Uncertainty reflects measurement errors, heterogeneous deformation, and variations in mineralogy and primary fabrics between cores. Uncertainty in mesoscopic structure orientations is typically

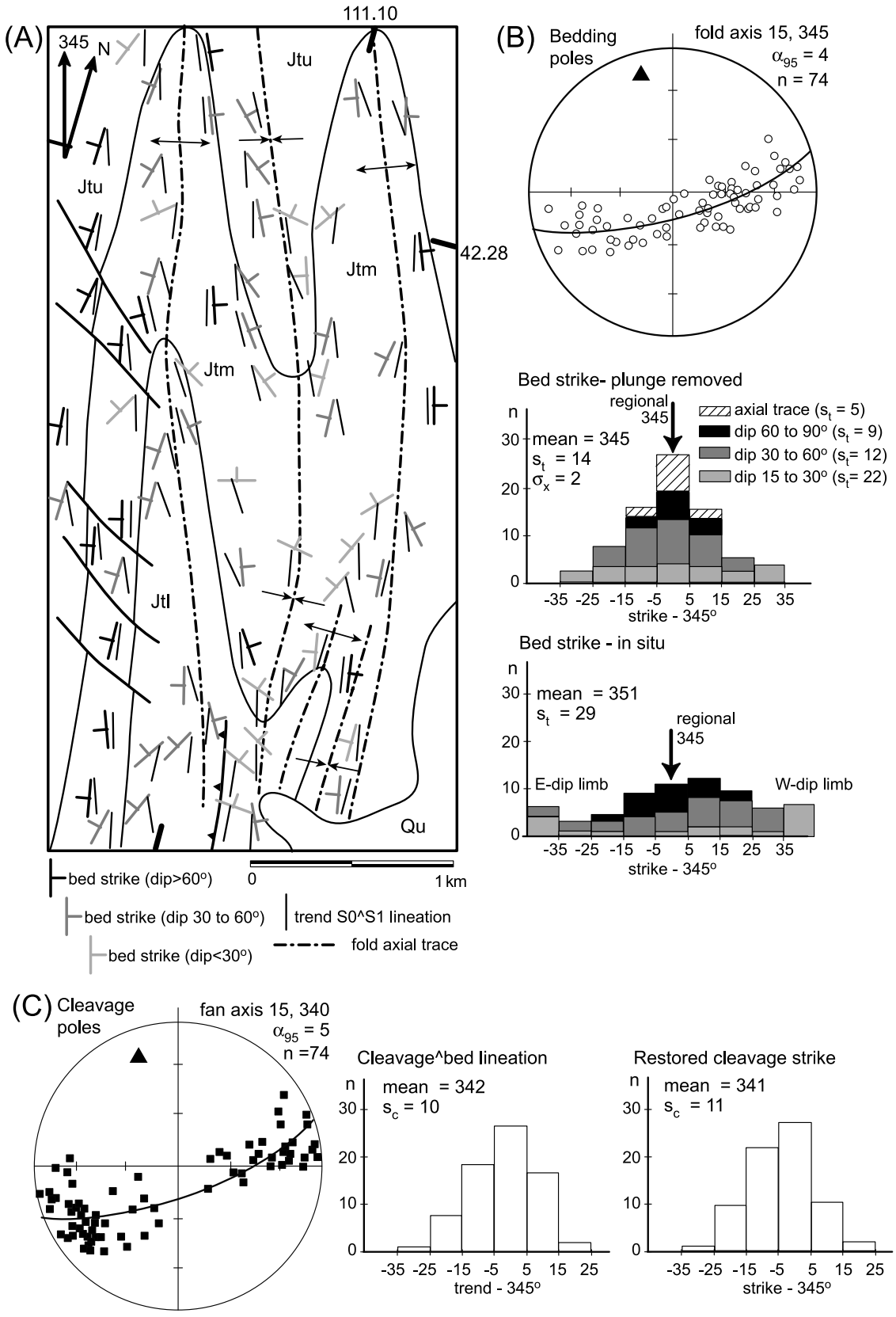
(A)
345 N
111.10
42.28
Jtu
Jtu
Jtm
Jtm
Jtl
Qu
bed strike (dip>60°)
bed strike (dip 30 to 60°)
bed strike (dip<30°)
0
1 km
trend S0^S1 lineation
fold axial trace
(B)
Bedding poles
fold axis 15, 345
α_{95} = 4
n = 74
Bed strike- plunge removed
regional 345
mean = 345
s_t = 14
σ_x = 2
axial trace (s_t = 5)
dip 60 to 90° (s_t = 9)
dip 30 to 60° (s_t= 12)
dip 15 to 30° (s_t= 22)
n
30
20
10
0
-35 -25 -15 -5 5 15 25 35
strike - 345°
Bed strike - in situ
mean = 351
s_t = 29
regional 345
E-dip limb
W-dip limb
strike - 345°
(C)
Cleavage poles
fan axis 15, 340
α_{95} = 5
n =74
Cleavage^bed lineation
mean = 342
s_c = 10
trend - 345°
Restored cleavage strike
mean = 341
s_c = 11
strike - 345°

Figure 4

evaluated from dispersion of individual readings using Bingham statistics. Dispersion reflects measurement errors and outcrop-scale variations partly related to material heterogeneity. For well defined fracture sets or cleavage, measuring 5 to 10 orientations at a site typically gives α_{95} cones of ~5 to 10°. Although AMS and mesoscopic structures provide useful proxies for strain directions in areas with simple deformation histories, relations may be more complex in areas where fabrics accumulated during multiple deformation increments.

[23] Structural noise, σ_n, related to random block rotation and stress/strain refraction at scales intermediate between individual sites and regional curvature produces additional variations in paleomagnetic and deformation fabric directions. Orientation analysis of cleavage at multiple subsites provides a way to estimate noise, as illustrated for a kilometer-scale study area in the Wyoming salient (Figure 4). Because strike tests only compare horizontal directions, residuals should be measured in a horizontal plane with fold plunge removed. Cleavage-bedding intersection lineations are typically at low angles to fold axes and not significantly effected by restoration of bed dip, and thus provide a direct measure of noise. Trends of lineations in the study area display an approximately normal distribution about the regional trend (Figure 4c), with residuals having a standard deviation of $s_c = 10°$, reflecting typical measurement error $\sigma_e \sim 5°$ and noise $\sigma_n \sim 8°$ (for $s_c^2 = \sigma_e^2 + \sigma_n^2$). Analysis of restored cleavage strike (with bedding returned to horizontal) yields a similar result. This example illustrates the importance of structural noise, which contributes to variations in deformation fabric directions between individual subsites. Although regional trend can commonly be closely estimated from averaging bedding/fold traces over kilometer-scale areas from existing geologic maps, detailed deformation fabric data are rarely available. Thus, structural noise determined for a detailed study area may need to be applied to other sites in regions with similar structural complexity.

[24] Due to the potentially complex nature of deformation paths in orogenic belts, care is needed in restoring in situ paleomagnetic and deformation fabric directions, using successive rotations based on structural and timing relations [*MacDonald*, 1980]. For complex structural settings (e.g., plunging and conical folds), incorrect restoration paths may introduce spurious components of apparent vertical axis rotation [*Pueyo et al.*, 2003]. Timing can be constrained by paleomagnetic fold/tilt tests, in which bedding is incrementally restored to horizontal and site directions are statistically evaluated to find at what stage of fold history maximum clustering occurs [*Weil and Van der Voo*, 2002]. In regions with distinctly curved structural trends, fold tests should be done on domains with consistent trend, or an inclination-only test should be used, which eliminates bias from differential vertical axis rotation between sites [*McFadden and Reid*, 1982]. For sites where bedding is subparallel to subhorizontal fold axes or dip panels above frontal thrust ramps, incremental rotation about bed strike is appropriate. Restoration of conical folds depends on local kinematic evolution, but lack of data on deformation paths may result in a range of restorations bracketed by end-member models [*Pueyo et al.*, 2003]. For sites located in simple settings with bedding restored by a single rotation about strike, the order of vertical axis rotation and unfolding does not affect restoration of prefolding paleomagnetic and deformation fabric directions, and $\sigma_p \approx 0°$ (Figure 5). For more complex cases (plunging or conical folds, and synfolding remagnetization), different restoration paths produce different paleomagnetic and deformation fabric directions, and thus may introduce spurious apparent rotations. Specifics vary in detail, but this effect is minor for gently dipping beds, but can be substantial ($\sigma_p > 10°$) for steep limbs of plunging or conical folds.

2.6. Structural Complexities and Filtered Data Sets

[25] Sites located near oblique ramps and transfer zones may experience more complex rotation histories and deformation partitioning [*Apotria et al.*, 1992; *Apotria*, 1995; *Wilkerson et al.*, 2002; *Bayona et al.*, 2003]. Steep to overturned fold limbs may experience greater strain and have more complex kinematic histories. Thus, sites located in structurally complex settings typically have larger uncertainties with nonnormal outliers. Therefore, strike tests on filtered data sets that only include sites from structurally simple settings may provide a better measure of regional rotation, which can be integrated with detailed analysis of sites from complex settings.

Figure 4. Regional structural trend and noise estimates for a study area in the Wyoming salient. (a) Generalized geologic map shows bedding strikes, trends of cleavage-bedding intersections (S0^S1), and fold axial traces. Units are Jtl, Jtm, Jtu, lower, middle, upper parts, respectively, of Jurassic Twin Creek Formation; and Qu, Quaternary deposits. Note map is drawn parallel to regional trend of 345°. Folds are upright and overall cylindrical with axial traces subparallel to regional trend but display increased shortening in SE part of area and are cut by tear faults in western part of area. Cleavage-bedding intersections are subparallel to regional trend but display local variation. (b) Analysis for determining regional structural trend. Stereogram of bedding poles has best fit fold axis of 15, 345°, and α_{95} confidence cone of 4°. Histogram of axial traces (measured over 1 km increments) and bedding strikes (corrected for plunge) has a mean trend of 345° and standard deviation of $s_t = 14°$. In detail, steep beds have smaller dispersion, whereas gentle beds have larger dispersion. Uncertainty in regional trend is $\sigma_x \approx s_t/\sqrt{n} = 2°$. Histogram of in situ bedding strike (not corrected for plunge) displays greater dispersion, with strike biased toward E/W along west dipping/east dipping limbs, respectively. Because more readings are from west dipping limbs, the mean strike is biased. (c) Analysis for determining structural noise. Stereogram of cleavage poles has best fit fan axis of 15, 340°, and α_{95} confidence cone of 5°. Histogram of cleavage-bedding intersection lineations has a mean of 342° and standard deviation of $s_c = 10°$. Histogram of restored cleavage strike has a mean of 341° and standard deviation of $s_c = 11°$. Dispersion reflects outcrop measurement error ($\sigma_e \sim 5°$) and structural noise $\sigma_n \sim 8°$ (for $s_c^2 = \sigma_n^2 + \sigma_e^2$).

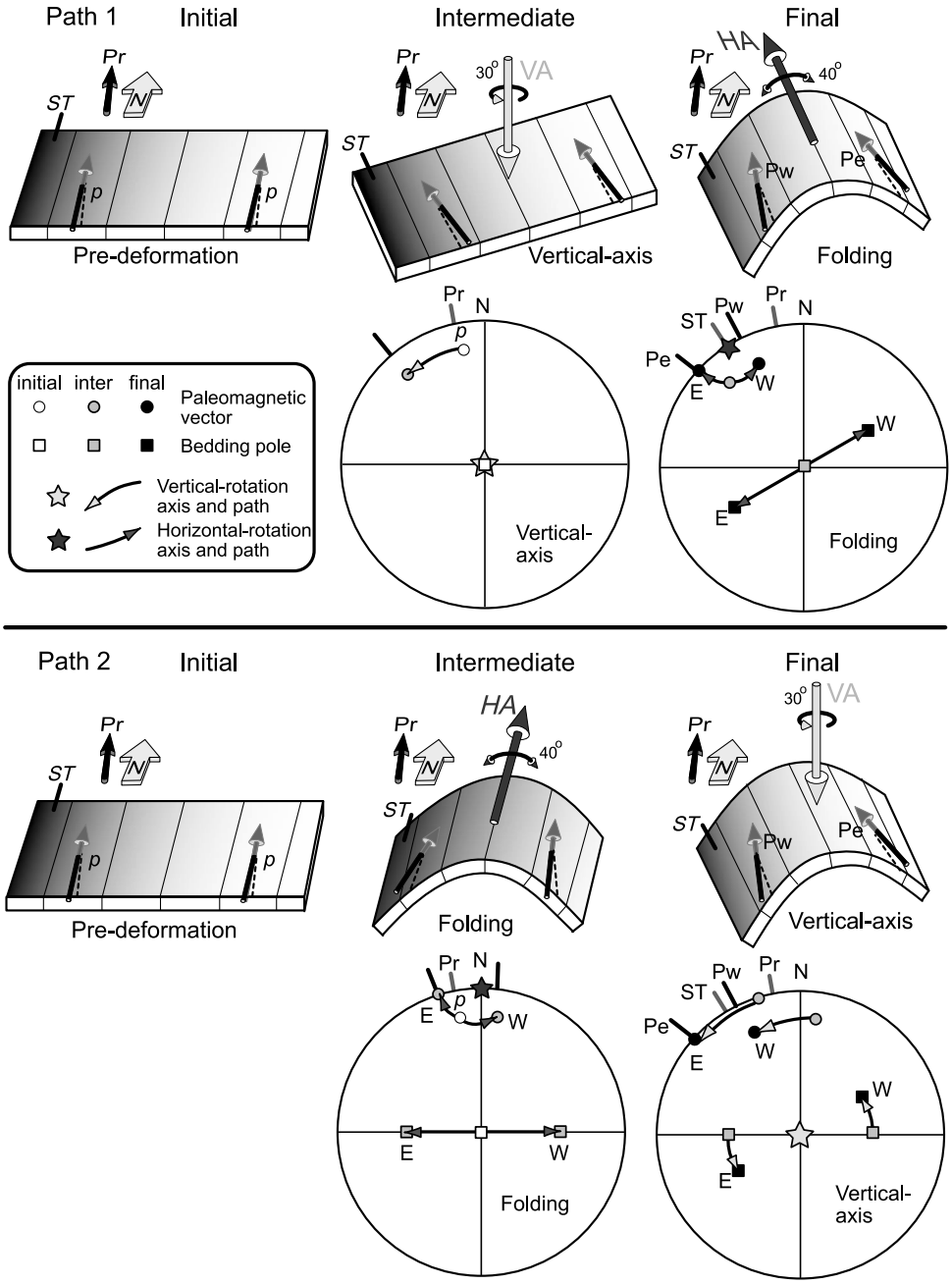

Figure 5. Rotations and restorations for the case of nonplunging, cylindrical folding. Inclined paleomagnetic vectors (*p*, initial, and Pe and Pw, final on east and west limbs of fold), reference declination (Pr), horizontal and vertical axis rotation axes (HA and VA), and structural trend (ST) indicated on shaded rock slabs. Initial state has north structural trend and NNW reference paleomagnetic declination. Final state has NW structural trend and fold. For path 1, intermediate vertical axis rotation is followed by horizontal folding about structural trend. For path 2, intermediate horizontal folding about structural trend is followed by vertical axis rotation. Final paleomagnetic vectors (black circles on stereograms) have the same orientations for both paths. The final paleomagnetic declinations are different on the two fold limbs (Pe and Pw); the apparent change in declination produced by folding must be restored to accurately estimate vertical axis rotation. For this simple case, the order of restoration does not affect estimates of vertical axis rotation. For plunging or conical folds, rotation order is not communicative, and incorrect restoration paths may introduce spurious (apparent) vertical axis rotation.

2.7. Summary

[26] Correlations between regional structural trend and changes in paleomagnetic (or deformation fabric) directions can be used to estimate vertical axis rotations with strike tests. A weighted least squares method, incorporating total site uncertainties, provides quantitative estimates of best fit slope, confidence intervals, and goodness of fit. Confidence intervals can be improved by increasing the number of sites, distributing sites over a wide range of structural trend, and decreasing site uncertainty through increased numbers of sample measurements. Total uncertainty in site directions reflects a combination of measurement dispersion, structural noise, and complex deformation paths, which must all be evaluated to obtain realistic weighting factors. Estimates of rotation require a reference direction. For paleomagnetic components that formed over a short interval, the reference direction is consistent for all sites. For deformation fabrics, however, strain trajectories may be initially curved, such that strike test slopes represent a combination of secondary rotation and initial fabric curvature. By integrating paleomagnetic and deformation fabric data sets, however, initial strain curvature can be quantified.

3. Case Study: Wyoming Salient, Sevier Thrust Belt

3.1. Geologic Setting

[27] The Wyoming salient is located within the Sevier thrust belt (Figure 6), which is characterized by folds and thrust faults that shortened and translated sedimentary rocks overall eastward during Early Cretaceous to Paleogene time [*Armstrong and Oriel*, 1965; *Royse*, 1993; *DeCelles*, 2004]. The salient is bound on the north and south by the basement-cored Gros Ventre and Uinta foreland uplifts. Major thrust systems in the salient, from west to east, are the: Willard (comprising the Willard, Paris, and Meade thrusts), Crawford (and associated fold system), Absaroka (and associated imbricates), and Hogsback (comprising the Hogsback, Darby, and Prospect thrusts). Major thrusts and associated folds display curvature over a range of scales, with regional structural trends curving from NW in the northern part to NE in the southern part of the salient, combined with local curvature near oblique thrust ramps and transfer zones (Figure 6). Synorogenic deposits and thermochronologic data record an overall foreland propagating (west to east) sequence of thrusts, from the Early Cretaceous Willard, to middle Cretaceous Crawford, to mostly Late Cretaceous Absaroka, to the early Paleogene Hogsback system [*Wiltschko and Dorr*, 1983; *Burtner and Nigrini*, 1994; *DeCelles*, 1994]. Cross sections through the salient, constrained by abundant seismic and drill hole data, illustrate typical fold-thrust structures [e.g., *Royse et al.*, 1975; *Blackstone*, 1977; *Dixon*, 1982; *Woodward*, 1986; *Coogan*, 1992; *Royse*, 1993]. Thrust-fold shortening decreases toward salient ends, and thrust slip directions change along regional trend.

[28] Frontal thrust systems (Crawford, Absaroka, and Hogsback) display systematic suites of deformation fabrics related to early layer-parallel shortening (LPS) and minor tangential extension [*Crosby*, 1969; *Mitra and Yonkee*, 1985; *Craddock et al.*, 1988; *Mitra*, 1994]. Shortening directions display an overall radial pattern subperpendicular to structural trend, which has been variously interpreted to record secondary rotation of initially consistent fabrics during curved thrust slip [*Craddock et al.*, 1988], or spreading of initially radial fabrics with no secondary rotation [*Crosby*, 1969]. This ambiguity illustrates the problem of interpreting rotation from structural data alone, as initial orientations must be known to estimate secondary rotation.

[29] Frontal thrust systems contain lithologies that carry stable remanent magnetic components, which can be used to quantify vertical axis rotations. Previous studies, however, have interpreted different patterns of vertical axis rotation. For example, *Grubbs and Van der Voo* [1976] interpreted significant rotations (up to 60°) for prefolding magnetizations in Triassic red beds within the northern frontal part of the salient, whereas *McWhinnie et al.* [1990] interpreted no significant vertical axis rotations in the same general area based on synfolding remagnetizations in Jurassic strata. To better understand the nature of curvature and resolve such inconsistencies, *Weil et al.* [2010], *Weil and Yonkee* [2009], and *Yonkee and Weil* [2010] conducted systematic paleomagnetic, AMS, and strain studies of the Wyoming salient. In section 3.2 we apply the weighted least squares method to integrated data sets from their papers, illustrating how rotation and uncertainties can be best estimated.

3.2. Sampling Design and Methods

[30] Paleomagnetic, finite strain, AMS, and structural data were collected and analyzed for 154 sites from red beds of the Triassic Ankareh Formation (Figure 6b). The formation consists mostly of quartzose to arkosic, variably calcareous mudstone and sandstone (Figure 7a). A conglomeratic interval divides the formation into an Early Triassic lower part and a Late Triassic upper part [*Kummel*, 1954; *High and Picard*, 1969]. Red beds contain hematite that grew during early diagenesis (Figure 7b), and display systematic mesoscopic structures, including cleavage, fracture sets, veins, and minor folds (Figure 7c). Sampling was designed to optimize site distribution along strike, with several detailed sampling arrays designed to check for local variations associated with folds and oblique ramps. Fold/tilt tests were performed on site data to establish the age of remanence acquisition, which is critical for evaluating the validity of paleomagnetically derived rotations. Individual thrust systems were sampled to evaluate temporal changes in rotation patterns. At each site, orientations of bedding and mesoscopic structures were measured, strain was estimated from reduction spots where available, and 6 to 10 oriented cores were drilled for paleomagnetic and AMS analysis.

[31] Structural trend for a site was obtained by analyzing bedding strikes, fold axial traces, and formation contacts (corrected for topography) over kilometer-scale areas on existing geologic maps (Figure 8a). Uncertainties in structural trend were small, $\sigma_x < 5°$, such that equations (1) and (2) were used for strike tests.

[32] Paleomagnetic components were determined by thermal demagnetization (Figure 8b), and included (1) a

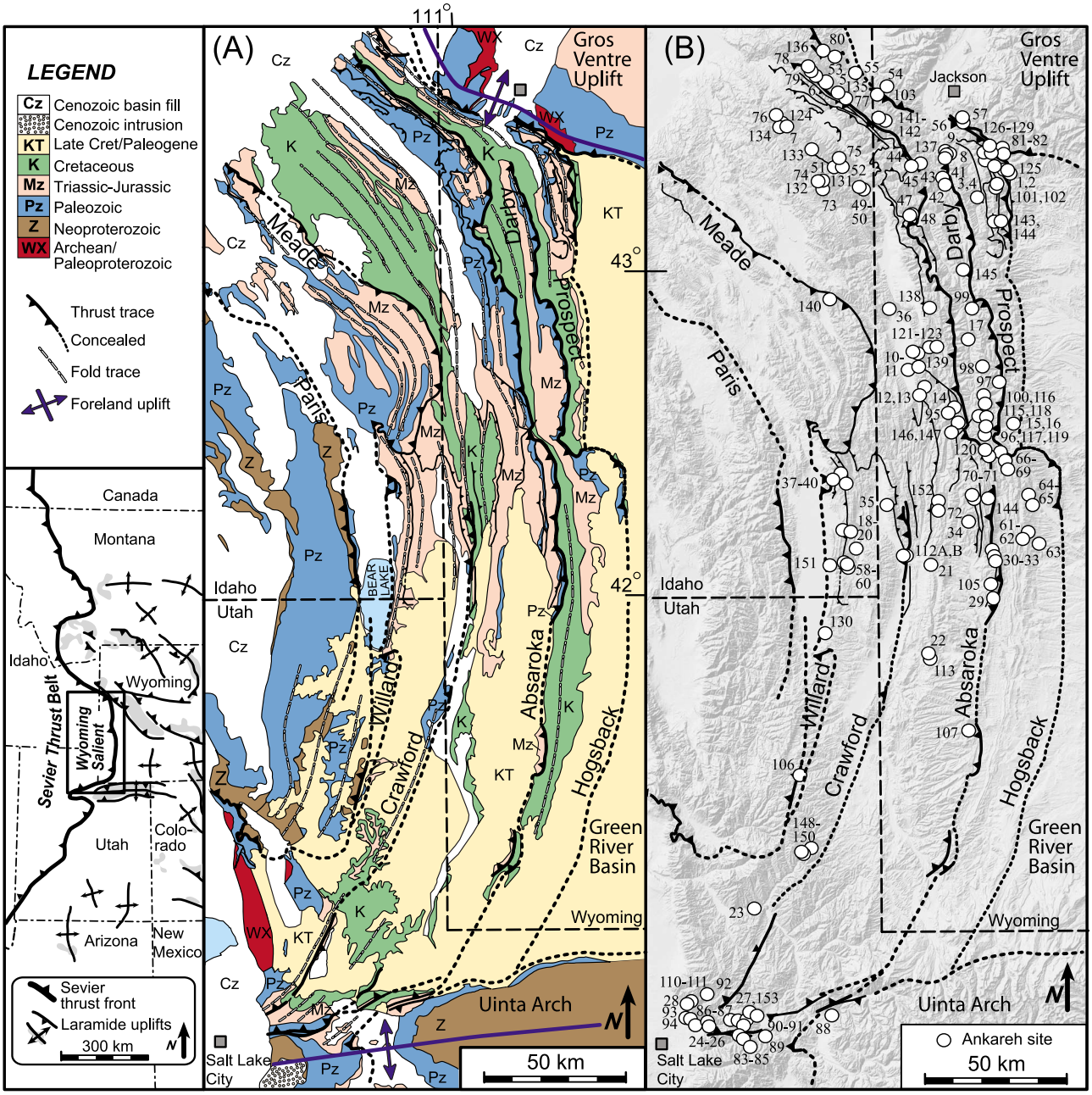

Figure 6. (a) Generalized geologic map and (b) shaded relief map of Wyoming salient with sample locations in Ankareh Formation labeled. Inset shows location of salient within the Sevier thrust belt. Major thrusts and folds display regional curvature from NW trends in the northern part to NE trends in the southern part of the salient. The salient is bound to the north and south by the foreland Gros Ventre and Uinta uplifts and to the east by the Green River Basin.

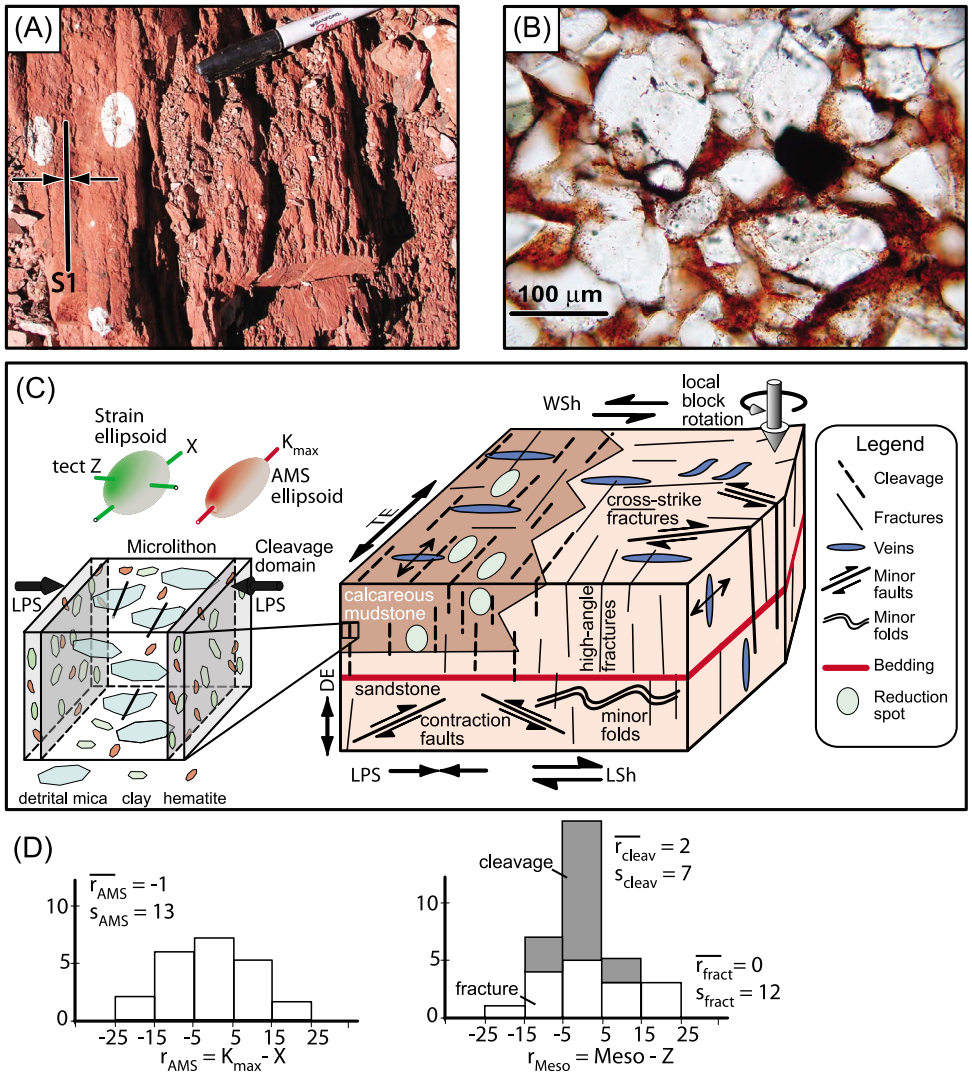

Figure 7. Structural style of Ankareh Formation. (a) Outcrop of calcareous fine-grained sandstone with cleavage (S1) related to LPS (arrows). Reduction spots are shortened perpendicular to cleavage. Pen for scale. (b) Photomicrograph of sandstone with hematite cement of quartz grains. Scale bar. (c) Block diagram illustration of typical relations of mesoscopic structures, including cleavage (dashed lines), fractures (thin lines), veins, minor faults (bold lines), and minor folds. Shapes of deformed reduction spots indicated by ellipses. Cleavage is subperpendicular to bedding, recording LPS and minor downdip extension (DE), with local refraction related to layer-parallel shear (LSh). High-angle fractures, related to partings along weak LPS fabrics, are also subperpendicular to bedding. Cross-strike fractures and associated veins record tangential extension (TE). Tear faults accommodated local wrench shear (WSh) and local block rotations. Small block to left shows relations of microtextures to the AMS and strain ellipsoids. AMS K_{max} is related to rotation of hematite and clay in thin cleavage domains and kinking of detrital mica that had an initial bedding fabric in microlithons. (d) Histograms of residuals between AMS K_{max} and finite strain X directions at individual sites from simple structure settings where both data are available and of residuals between cleavage/high-angle fracture poles and tectonic Z (shortening) directions. Means of residuals are ~0, and standard deviations reflect measurement error, along with additional fabric variability for AMS and fracture data.

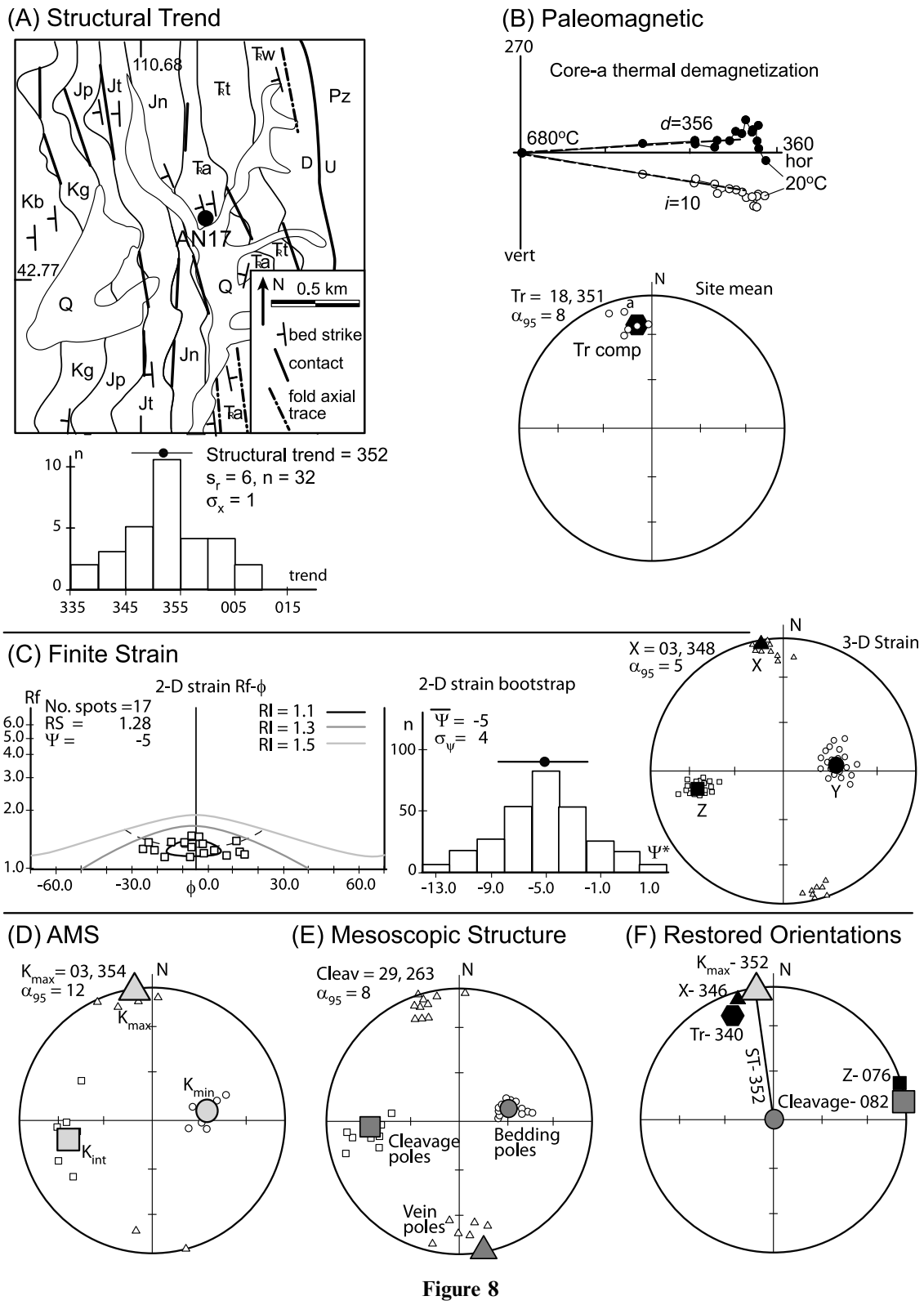
(A) Structural Trend
110.68
Jp
Jt
Jn
Tkt
Tkw
Pz
D
U
Kb
Kg
Tka
AN17
42.77
Q
Tkl
N
0.5 km
bed strike
contact
fold axial trace
Structural trend = 352
s_r = 6, n = 32
σ_x = 1
n
trend
335 345 355 005 015
(B) Paleomagnetic
270
Core-a thermal demagnetization
d=356
680°C
360
hor
20°C
i=10
vert
Tr = 18, 351
α_{95} = 8
Site mean
Tr comp
(C) Finite Strain
2-D strain Rf-ϕ
Rf
No. spots =17
RS = 1.28
Ψ = -5
Rl = 1.1
Rl = 1.3
Rl = 1.5
2-D strain bootstrap
$\overline{\Psi}$ = -5
σ_ψ = 4
Ψ*
X = 03, 348
α_{95} = 5
3-D Strain
X
Y
Z
(D) AMS
K_{max} = 03, 354
α_{95} = 12
K_{max}
K_{min}
K_{int}
(E) Mesoscopic Structure
Cleav = 29, 263
α_{95} = 8
Cleavage poles
Bedding poles
Vein poles
(F) Restored Orientations
K_{max}- 352
X- 346
Tr- 340
ST- 352
Z- 076
Cleavage- 082

Figure 8

near-primary Triassic (Tr) component carried by diagenetic hematite; (2) a Cretaceous (K) remagnetization component carried partly by magnetite that likely formed during a regional hydrothermal event; and (3) a present-day viscous overprint generally removed by 350°C [*Weil et al.*, 2010]. Remanence directions for individual cores were calculated using principal component analysis from orthogonally projected demagnetization plots [*Zijderveld*, 1967; *Torsvik et al.*, 1999]. In situ vector means and α_{95} cones were calculated from core directions using the method of *Fisher* [1953]. The average restored inclination, i, was ~20° for the Tr component and ~60° for the K component, both consistent with estimated paleolatitudes of North America in the Triassic to Cretaceous. Uncertainties in site mean declinations (given by $\sigma_m \approx 0.4*\alpha_{95}/\cos(i)$ [*Demarest*, 1983]) were typically 4–7° for the Tr component and 7–12° for the more steeply inclined K component, corresponding to typical α_{95} cones of 8–15°.

[33] Finite strain was estimated from reduction spots (Figure 8c), which varied from essentially undeformed in central parts of the Hogsback system to distinctly elliptical toward the west [*Yonkee and Weil*, 2010]. Where present, 15 to 30 spots were measured on each of three approximately perpendicular surfaces. Two-dimensional fabric ellipses were calculated using the Rf-ϕ tensor method [*Shimamoto and Ikeda*, 1976], with uncertainties evaluated using bootstrap resampling. Principal directions and ratios of 3-D fabric ellipsoids were calculated from 2-D data, with uncertainties evaluated using Monte Carlo simulations following *Yonkee* [2005]. The final ellipsoid reflects both a primary sedimentary fabric and tectonic strain. At the least deformed sites, reduction spots defined slightly oblate ellipsoids parallel to bedding, related to sedimentary compaction. At low strain sites, reduction spots defined prolate ellipsoids with long (X) axes broadly parallel to the intersection of weak LPS fabrics with bedding. At moderate to higher strain, ellipsoids became triaxial, with tectonic shortening (Z) axes perpendicular to cleavage and X axes subparallel to the intersection of cleavage with bedding.

[34] AMS data were collected for 6 to 10 cores per site using a susceptibility bridge [*Weil and Yonkee*, 2009]. Core data were analyzed using the parametric bootstrap approach of *Tauxe* [1998] to estimate principal directions, ratios, and 95% confidence angles of the 3-D AMS ellipsoid (Figure 8d). AMS ellipsoids in the Ankareh Formation are similar to those observed in weakly to moderately deformed sedimentary rocks from other thrust belts [e.g., *Borradaile and Tarling*, 1981, 1984; *Kissel et al.*, 1986; *Averbuch et al.*, 1992; *Parés and Dinarès Turell*, 1993; *Sagnotti and Speranza*, 1993; *Parés et al.*, 1999]. The least deformed sites displayed oblate ellipsoids parallel to bedding, related to a dominant sedimentary fabric. Low strain sites had ellipsoids with a weak magnetic lineation (K_{max}) broadly parallel to the intersection of weak LPS fabrics with bedding. With increasing strain, sites had moderate-intensity K_{max} clustered subparallel to the intersection of strengthening LPS fabrics with bedding. A few sites had AMS fabrics oblique to bedding. Uncertainties in gently inclined K_{max} directions (estimated using a parametric bootstrap) were mostly 3–10° for sites with definable lineations; K_{max} was poorly constrained for sites with a dominant sedimentary fabric. Note, AMS records a composite of deformation and sedimentary fabrics, producing additional 'fabric variability' compared to finite strain directions. Angular residuals between finite strain X and AMS K_{max} directions for sites where data were available ($r_{AMS} = K_{max} - X$ trend) had a mean ≈ 0, indicating AMS is an unbiased proxy, and a standard deviation s_r = 13°, reflecting a combination of measurement uncertainty (σ_m ~ 8°) and fabric variability (σ_f ~ 10°, given by $s_r^2 = \sigma_m^2 + \sigma_f^2$; Figure 7d).

[35] Orientations of bedding, cleavage, and fracture/vein sets were measured for each site (Figure 8e) [*Yonkee and Weil*, 2010]. Vector mean orientations and α_{95} cones were calculated using the orientation tensor method of *Hext*

Figure 8. Example data sets for site AN17. (a) Geologic map of area modified from *Rubey* [1973] showing bed strikes, formation contacts, and fold axial traces used to estimate structural trend. Histogram of strikes, contacts, and traces shows a mean trend of 352° and uncertainty σ_x = 1° (for standard deviation s_t = 6° and n = 32 readings). Units are Pz, undivided Paleozoic strata; Trw, Triassic Woodside; Trt, Thaynes; Tra, Ankareh; Jn, Jurassic Nugget; Jt, Twin Creek; Jp, Preuss; Kg, Cretaceous Gannett; and Kb, Bear River Formation; Q, Quaternary deposits. (b) In situ paleomagnetic data. Thermal demagnetization plot for core (a) shows linear segments with fit declination (d) and inclination (i) components indicated; radial distance scaled to intensity. Stereogram shows site mean for Triassic component (hexagon scaled to α_{95}) and individual core values (circles). Site mean and α_{95} calculated using Fisher statistics. (c) In situ finite strain data. Rf-ϕ plot for reduction spots along bed-parallel surface, with 2-D strain ratio (RS = 1.28) and stretching direction (Ψ = −5°, rake from bedding strike) calculated using tensor method. Curves plotted for various initial ratios (RI) indicate that reduction spots started close to circular. Histogram of bootstrap resample directions (Ψ*) has a mean of −5° with an uncertainty of 4°. Stereogram shows best fit 3-D strain directions (X > Y > Z, solid symbols scaled to α_{95}) calculated from 2-D data for three planes and 20 Monte Carlo simulations (open symbols). Principal directions and α_{95} calculated using approach of *Yonkee* [2005]. (d) In situ AMS data. Stereogram shows site-mean principal directions (solid symbols scaled to α_{95}) and individual core directions (open symbols). Mean directions and α_{95} calculated using parametric bootstrap method of *Tauxe* [1998]. (e) In situ mesoscopic structural data. Stereogram shows poles to bedding (open circles), poles to cleavage and high-angle fractures (open squares), and poles to cross-strike veins and fractures (open triangles). Mean values shown by solid symbols (scaled to α_{95}). Mean directions and α_{95} calculated using *Bingham* [1984] statistics. (f) Restored site-mean directions (for single rotation about strike to restore bedding to horizontal). Restored directions are listed. The restored Tr component declination is −10° relative to the reference Late Triassic paleomagnetic direction of 350°, and restored X, K_{max}, and cleavage pole directions range from −8° to −14° relative to N-S/E-W reference directions.

[1963]. Fractures were not statistically analyzed for sites where limited outcrop size prevented identification of systematic sets. Cleavage is typically subperpendicular to bedding and formed during early LPS prior to large-scale folding (Figure 7c). Cleavage is better developed in calcareous mudstone, and within more interior thrust systems. Fractures are widely developed in sandstone, with most sites displaying two dominant sets: one at high angles to bedding and subparallel to structural trend (high-angle set); and a second subperpendicular to structural trend (cross-strike set; Figure 7c). The high-angle set partly reflects partings along weak LPS fabrics, but some sites have subsests at acute (~10–20°) angles to each other that record block rotation or stress changes during progressive deformation, and some fractures may have formed during folding and thrusting. Cross-strike fractures and associated veins record minor tangential extension. Tear faults and en echelon vein arrays record local wrench shear. A few sites have additional fractures oblique to structural trend, especially near oblique ramps. Measurement uncertainties in gently inclined cleavage/fracture poles were typically 2–4°.

[36] Angular residuals between tectonic Z and cleavage pole directions for sites where data were available (r_{clear} = cleavage pole − Z trend) had a mean ≈ 0° and a standard deviation of s_r = 7° related to measurement uncertainty, indicating that cleavage is a good proxy for strain directions (Figure 7d). Angular residuals between tectonic Z and high-angle fracture directions had larger standard deviation of s_r = 12°, reflecting combined measurement uncertainty ($\sigma_m \sim 8°$) and fabric variability ($\sigma_f \sim 8°$) related to fracturing during multiple deformation increments. Fabric variability can be thought of as an addition to measurement uncertainty for individual site samples that do not adequately represent total fabric dispersion.

[37] Structural noise between sites also contributes to total uncertainty. Although the Ankareh Formation is exposed at individual sites, large exposures are rare as the formation is relatively nonresistant to weathering. Limestone of the Jurassic Twin Creek Formation, which displays a similar structural style, however, is well exposed in parts of the Wyoming salient. Statistical analysis of cleavage orientations over kilometer-scale areas yielded an estimate for structural noise of $\sigma_n \sim 8°$ (Figure 4c), which is comparable to measurement uncertainties, and thus is an important contribution to weighting factors.

[38] Due to the complex deformation history in the salient, care was taken to restore paleomagnetic and deformation fabric directions to their initial orientations (Figure 8f). Fold tests were conducted for Tr and K paleomagnetic components to determine timing relations. Clustering of inclinations was maximum for 100% unfolding of the Tr component and for 80 to 90% unfolding of the K component [*Weil et al.*, 2010]. Reference paleomagnetic directions of 340° and 350° were used for sites from the Early Triassic lower part and Late Triassic upper part of the Ankareh Formation, with 350° used for sites that carried the K component [*Weil et al.*, 2010]. Cleavage and related fabrics that formed during early LPS were restored by 100% unfolding. Most sites were located in relatively simple settings with bedding restored by a single rotation about strike. However, some sites had more complex paths that included removal of fold plunge or partial unfolding of the K component. In this case, estimates of initial orientation depended on the restoration path; this effect was minor ($\sigma_p < 5°$) for gently dipping beds, but was substantial ($\sigma_p > 10°$) for steep limbs of plunging folds.

[39] Of the 154 sites collected in the Ankareh Formation, 125 were located in relatively simple structural settings, 27 were from complex settings (oblique ramps, transfer zones, overturned fold limbs), and 2 sites were from adjacent margins of foreland uplifts. Overturned fold limbs and oblique ramps have greater internal deformation and more complex rotation histories, resulting in larger uncertainties. Herein we only report results for filtered data sets from structurally simple settings. Analysis of rotation patterns for complex areas is given by *Weil et al.* [2010] and *Yonkee and Weil* [2010]. From equation (8), the expected number of sites needed to provide a 95% confidence interval of 0.1 is $N \approx 60$, for the 90° range in structural trend of the Wyoming salient and $\sigma_y \approx 10°$ (typical site uncertainty). Thus, the number of sites should be adequate to closely constrain regional rotation patterns.

3.3. Results for Paleomagnetic Analysis

[40] The Ankareh Formation contained 85 sites that preserved a well defined Tr paleomagnetic component, and 29 sites that preserved the early synfolding K component; the remaining sites had a strong viscous present-day overprint, displayed high dispersion of core values ($\alpha_{95} > 15°$), or had experienced high strain (Table 1). Of sites that carried the Tr component, 65 were located in relatively simple structural settings, and 22 of the sites that carried the K component were located in simple settings. Declinations of restored paleomagnetic site means for both the Tr and K components display systematic regional variations around the Wyoming salient (Figure 9a) [*Weil et al.*, 2010]. Sites in the northern part of the salient record counterclockwise rotations, sites in the central part of the salient record only minor rotations, and sites in the southern part of the salient record clockwise rotations. Broadly similar rotation patterns are apparent in all of the studied thrust systems. In detail, restored declinations display minor (±10°) scatter for sites in similar structural domains, related to measurement uncertainties and structural noise.

[41] Least squares analysis of the 65 filtered Tr sites from all thrust systems yielded a slope of 0.75 ± 0.11 (at a 95% confidence interval), determined for weighting factors related to measurement uncertainty and structural noise (Figure 10a). Residuals had a quasi-normal distribution with a standard deviation, s_r = 11°, and gave a marginally acceptable goodness of fit. Observed scatter in residuals reflected measurement uncertainty in site means ($\sigma_m \sim 4$–7°) and structural noise ($\sigma_n \sim 8°$). Ignoring structural noise ($\sigma_n = 0$) yielded the same slope with an apparently reduced confidence interval of ±0.06, but gave an unacceptably poor goodness of fit ($Q < 0.01$). The poor fit results from residuals being greater than measurement uncertainty alone.

Table 1. Paleomagnetic and Deformation Fabric Data for Ankareh Formation, Wyoming Salient[a]

			Structure							
Site	Lat	Long	Thrust	Setting	Bedding	Trend	Paleomag[b]	Strain	AMS	LPS Dir
AN-01	43.272	110.525	H	s	270, 20 (±3)	340	ha	-	345 (±3)	250 (±2)
AN-02	43.283	110.535	H	s	245, 48 (±3)	340	pd	338 (±4)	sf	245 (±3)
AN-03	43.287	110.570	H	s	232, 27 (±4)	341	ha	-	343 (±4)	233 (±3)
AN-04	43.287	110.570	H	s	068, 64 (±4)	341	356 (±5)^{tu}	-	342 (±4)	of
AN-05	43.596	111.224	H	s, p	196, 60 (±3)	311	335 (±11)^{k}	-	296 (±3)	218 (±2)
AN-06	43.553	111.299	H	s	224, 68 (±5)	315	329 (±5)^{tu}	-	343 (±3)	240 (±5)
AN-07	43.410	111.437	C	s	226, 45 (±6)	317	350 (±10)^{k}	-	-	-
AN-08	43.324	110.770	H	s, p	051, 62 (±4)	328	322 (±4)^{tu}	338 (±4)	-	225 (±2)
AN-09	43.330	110.786	H	s	324, 36 (±5)	330	ni	-	ni	-
AN-10	42.684	110.913	A	s	084, 47 (±4)	352	339 (±11)^{k}	-	017 (±3)	247 (±4)
AN-11	42.684	110.902	A	s	259, 52 (±3)	352	355 (±7)^{k}	-	356 (±4)	-
AN-12	42.610	110.881	A	s	277, 44 (±4)	360	342 (±7)^{k}	359 (±3)	-	265 (±4)
AN-13	42.630	110.850	A	s	271, 45 (±5)	360	353 (±5)^{tu}	-	of	278 (±3)
AN-14	42.567	110.735	A	s	257, 38 (±4)	347	345 (±5)^{tu}	-	346 (±4)	243 (±3)
AN-15	42.510	110.495	H	s	245, 25 (±7)	347	ha	-	sf	245 (±2)
AN-16	*42.511*	*110.492*	*H*	*c*	*077, 93 (±3)*	*347*	*015 (±4)^{tu}*	-	*352 (±8)*	*264 (±5)*
AN-17	42.773	110.676	H	s	255, 33 (±3)	352	340 (±4)^{tu}	346 (±4)	352 (±8)	262 (±4)
AN-18	42.198	111.164	C	s	266, 40 (±4)	355	ha	352 (±3)	sf	251 (±2)
AN-19	*42.200*	*111.175*	*C*	*c*	*066, 94 (±3)*	*355*	*355 (±6)^{tu}*	-	*333 (±2)*	*236 (±2)*
AN-20	42.135	111.146	C	s, p	074, 57 (±4)	003	009 (±4)^{tu}	-	325 (±3)	-
AN-21	42.103	110.841	A	s	274, 52 (±3)	005	356 (±4)^{tu} 346 (±8)^{k}	009 (±3)	349 (±7)	292 (±2)
AN-22	*41.832*	*110.837*	*A*	*c*	*217, 19 (±2)*	*~005*	*ni*	-	-	*of*
AN-23	41.065	111.559	C	s	103, 77 (±2)	015	358 (±5)^{tu} 043 (±11)^{k}	-	029 (±3)	288 (±5)
AN-24	40.709	111.795	C	s, r	336, 71 (±3)	015	hs	002 (±5)	of	281 (±4)
AN-25	40.706	111.610	C	s, r	080, 39 (±6)	020	ni	-	049 (±2)	-
AN-26	40.719	111.652	C	s, r	340, 62 (±8)	018	347 (±4)^{tu}	-	015 (±2)	278 (±3)
AN-27	40.747	111.580	C	s, r	359, 60 (±5)	025	345 (±4)^{tl}	-	015 (±2)	276 (±4)
AN-28	40.771	111.818	C	s, r	151, 45 (±4)	058	ha	-	052 (±2)	-
AN-29	42.035	110.590	A	s	273, 80 (±5)	012	015 (±7)^{k}	-	sf	-
AN-30	42.109	110.592	A	s	282, 50 (±4)	005	ha	sf	sf	285 (±3)
AN-31	*42.123*	*110.596*	*A*	*c*	*220, 57 (±5)*	*~360*	*002 (±10)^{k}*	-	*sf*	*268 (±5)*
AN-32	*42.135*	*110.611*	*A*	*c*	*245, 43 (±4)*	*~360*	*360 (±10)^{k}*	-	*sf*	-
AN-33	42.140	110.603	A	s	283, 28 (±4)	360	358 (±11)^{k}	-	sf	-
AN-34	42.230	110.682	A	s	276, 35 (±5)	360	360 (±11)^{k}	-	sf	268 (±5)
AN-35	*42.277*	*111.008*	*C*	*c*	*101, 94 (±5)*	*010*	*348 (±6)^{tu} 019 (±11)^{k}*	*011 (±3)*	*345 (±3)*	*286 (±5)*
AN-36	42.859	110.994	C	s	066, 69 (±5)	348	001 (±8)^{k}	338 (±3)	ni	242 (±5)
AN-37	*42.340*	*111.188*	*C*	*c*	*061, 113 (±6)*	*344*	*349 (±6)^{tl}*	*332 (±3)*	*347 (±8)*	-
AN-38	42.373	111.204	C	s, p	296, 14 (±4)	334	ha	-	of	243 (±3)
AN-39	42.369	111.207	C	s, p	329, 28 (±5)	335	313 (±5)^{tl}	-	331 (±3)	240 (±5)
AN-40	42.353	111.222	C	s, p	037, 20 (±3)	335	316 (±7)^{tl}	-	314 (±3)	247 (±2)
AN-41	43.230	110.773	H	s	250, 40 (±5)	340	322 (±4)^{tu}	-	321 (±5)	-
AN-42	43.250	110.780	H	s	260, 29 (±4)	345	319 (±7)^{tu}	-	323 (±3)	238 (±3)
AN-43	43.315	110.785	H	s, p	282, 52 (±7)	342	358 (±6)^{tu}	-	329 (±5)	267 (±3)
AN-44	*43.292*	*110.870*	*A*	*c*	*057, 106 (±5)*	*335*	*349 (±7)^{tu}*	-	*302 (±6)*	*243 (±3)*
AN-45	43.289	110.875	A	s	029, 12 (±3)	335	ni	-	-	219 (±2)
AN-46	43.285	110.887	A	s, p	294, 41 (±8)	335	315 (±7)^{tu}	-	344 (±3)	224 (±3)
AN-47	43.143	110.913	A	s	238, 37 (±4)	332	311 (±7)^{tu}	-	340 (±5)	246 (±3)
AN-48	43.143	110.912	A	s	237, 48 (±3)	332	323 (±6)^{tu}	-	337 (±3)	260 (±3)
AN-49	43.223	111.117	C	s	082, 62 (±4)	340	337 (±7)^{tu}	342 (±3)	349 (±4)	240 (±4)
AN-50	43.219	111.112	C	s	225, 18 (±3)	335	pd	342 (±3)	353 (±3)	248 (±4)
AN-51	43.278	111.228	C	s, p	208, 43 (±4)	327	328 (±4)^{tu}	-	337 (±4)	240 (±3)
AN-52	*43.298*	*111.198*	*C*	*c*	*005, 156 (±5)*	*327*	*ha*	-	*355 (±5)*	-
AN-53	43.534	111.264	A	s, p	220, 70 (±3)	317	ha	-	310 (±6)	227 (±5)
AN-54	*43.532*	*111.022*	*F*	*f*	*209, 127 (±4)*	-	*351 (±4)^{tu}*	-	*343 (±9)*	*217 (±4)*
AN-55	43.564	111.142	H	s	240, 33 (±3)	327	hs	332 (±4)	325 (±6)	235 (±2)
AN-56	43.423	110.702	H	s	034, 61 (±6)	318	ni	-	337 (±6)	-
AN-57	43.420	110.706	H	s	225, 50 (±4)	318	328 (±6)^{tu}	-	317 (±9)	249 (±3)
AN-58	42.095	111.181	C	s	277, 47 (±4)	007	340 (±6)^{tl}	-	354 (±4)	270 (±3)
AN-59	42.105	111.193	C	s	277, 43 (±6)	358	pd	-	354 (±9)	261 (±4)
AN-60	42.106	111.191	C	s	071, 28 (±5)	358	pd	-	011 (±6)	275 (±3)
AN-61	42.196	110.444	H	s	103, 36 (±4)	010	357 (±5)^{k}	-	359 (±4)	280 (±4)
AN-62	*42.178*	*110.460*	*H*	*c*	*195, 30 (±8)*	*~005*	*002 (±3)^{tu}*	-	*of*	-
AN-63	42.150	110.392	H	s	267, 28 (±4)	005	005 (±5)^{tu}	-	sf	of
AN-64	42.280	110.421	H	s	267, 40 (±5)	360	344 (±4)^{tu}	-	336 (±8)	264 (±4)
AN-65	42.306	110.454	H	s	086, 21 (±3)	360	354 (±7)^{tu}	sf	sf	269 (±4)
AN-66	*42.389*	*110.522*	*H*	*c*	*239, 33 (±3)*	*~360*	*353 (±3)^{tl}*	*346 (±4)*	*333 (±4)*	*of*
AN-67	42.409	110.529	H	s	271, 41 (±3)	005	346 (±6)^{tl}	sf	sf	of
AN-68	*42.436*	*110.547*	*H*	*c*	*230, 44 (±5)*	*~360*	*009 (±7)^{k}*	-	-	*289 (±5)*

Table 1. (continued)

Site	Lat	Long	Structure		Bedding	Trend	Paleomag[b]	Strain	AMS	LPS Dir
			Thrust	Setting						
AN-69	42.433	110.623	H	s	252, 42 (±4)	335	ni	-	-	222 (±3)
AN-70	42.299	110.674	A	s	218, 19 (±6)	355	344 (±7)[tu]	-	sf	of
AN-71	42.296	110.673	A	s	250, 22 (±3)	355	355 (±3)[tu]	-	-	250 (±3)
AN-72	42.262	110.798	A	s	267, 35 (±4)	360	ha	-	ni	260 (±2)
AN-73	43.228	111.254	C	s	067, 91 (±3)	324	hs	343 (±4)	350 (±2)	240 (±2)
AN-74	43.236	111.271	C	s	236, 38 (±3)	324	321 (±9)[k]	323 (±3)	314 (±7)	231 (±2)
AN-75	*43.307*	*111.205*	*C*	*c*	*047, 145 (±4)*	*320*	*315 (±7)[k]*	-	*304 (±5)*	*212 (±4)*
AN-76	43.433	111.460	C	s	238, 37 (±3)	319	299 (±8)[k]	-	sf	227 (±2)
AN-77	43.509	111.204	A	s	237, 69 (±−3)	310	pd	-	282 (±4)	218 (±2)
AN-78	43.576	111.326	A	s	060, 47 (±3)	325	289 (±7)[tu]	-	299 (±7)	-
AN-79	43.574	111.320	A	s	229, 46 (±2)	325	310 (±4)[tu]	-	357 (±9)	233 (±2)
AN-80	43.631	111.273	H	s	227, 41 (±3)	317	hs	331 (±3)	321 (±3)	227 (±3)
AN-81	*43.326*	*110.519*	*H*	*c*	*065, 106 (±3)*	*335*	*329 (±5)[tu]*	-	-	-
AN-82	43.338	110.537	H	s, r	195, 82 (±3)	335	330 (±4)[tu]	-	315 (±7)	232 (±2)
AN-83	40.645	111.579	A	s, r	039, 21 (±3)	030	ha	028 (±4)	-	284 (±2)
AN-84	40.669	111.607	A	s, r	113, 63 (±5)	036	hs	042 (±4)	-	309 (±2)
AN-85	40.672	111.612	A	s, r	328, 47 (±4)	036	015 (±4)[tl]	-	044 (±2)	329 (±2)
AN-86	40.717	111.749	A	s, r	084, 52 (±6)	028	hs	029 (±4)	-	303 (±2)
AN-87	40.710	111.740	A	s, r	332, 52 (±4)	028	018 (±4)[tl]	-	-	296 (±2)
AN-88	*40.742*	*111.239*	*F*	*f*	*333, 36 (±3)*	-	*352 (±4)[tu]*	-	-	*323 (±2)*
AN-89	40.676	111.520	A	s, r	358, 36 (±2)	021	343 (±4)[tl]	023 (±3)	032 (±3)	290 (±3)
AN-90	*40.729*	*111.594*	*A*	*c*	*026, 109 (±4)*	*040*	*ha*	-	*of*	*317 (±4)*
AN-91	40.738	111.553	A	s, r	072, 51 (±4)	042	ha	-	040 (±9)	297 (±3)
AN-92	40.804	111.749	C	s, r	159, 71 (±3)	060	051 (±5)[tu]	-	061 (±2)	-
AN-93	40.738	111.806	C	s, r	325, 78 (±2)	049	057 (±11)[k]	-	049 (±2)	315 (±3)
AN-94	*40.724*	*111.805*	*C*	*c*	*135, 82 (±4)*	*049*	*084 (±4)[tu]*	-	*025 (±8)*	*331 (±2)*
AN-95	42.546	110.761	A	s	256, 72 (±2)	340	346 (±4)[tu] 328 (±8)[k]	-	sf	268 (±2)
AN-96	*42.489*	*110.618*	*H*	*c*	*195, 39 (±3)*	*~345*	*ni*	-	*342 (±5)*	*248 (±3)*
AN-97	42.643	110.559	H	s	262, 61 (±3)	355	015 (±5)[tu] 004 (±8)[k]	345 (±4)	sf	246 (±3)
AN-98	42.671	110.628	H	s	067, 07 (±2)	360	357 (±7)[tu]	-	sf	257 (±4)
AN-99	42.866	110.682	H	s	287, 31 (±2)	356	329 (±5)[tu]	-	346 (±4)	275 (±3)
AN-100	42.603	110.625	H	s	357, 06 (±3)	360	334 (±7)[tu]	-	of	271 (±2)
AN-101	*43.221*	*110.566*	*H*	*c*	*264, 30 (±3)*	*~010*	*035 (±7)[tu]*	-	*of*	*295 (±2)*
AN-102	43.224	110.558	H	s	114, 35 (±4)	~010	ha	005 (±4)	ni	289 (±3)
AN-103	43.504	110.051	H	s	292, 124 (±4)	295	304 (±6)[tu]	-	296 (±4)	214 (±3)
AN-104	43.210	110.649	H	s	266, 30 (±3)	355	-	341 (±3)	-	264 (±3)
AN-105	41.995	110.605	A	s	279, 84 (±3)	010	321 (±5)[tu]	-	sf	-
AN-106	*41.457*	*111.382*	*C*	*c*	*101, 142 (±4)*	*008*	*039 (±6)[tu]*	-	*sf*	*285 (±4)*
AN-107	*41.604*	*110.684*	*A*	*c*	*224, 75 (±3)*	*~010*	*037 (±4)[tu]*	-	*031 (±3)*	*278 (±3)*
AN-108	40.475	111.516	A	s	132, 18 (±3)	025	ha	-	of	281 (±3)
AN-109	*40.460*	*111.533*	*A*	*c*	*152, 33 (±4)*	*~035*	*354 (±6)[tl]*	-	*012 (±4)*	*290 (±2)*
AN-110	40.779	111.815	C	s	135, 32 (±2)	051	035 (±6)[tl]	-	042 (±2)	322 (±2)
AN-111	40.771	111.822	C	s	162, 41 (±2)	055	011 (±7)[tl]	-	047 (±2)	338 (±2)
AN112A	42.124	110.940	C	s	061, 28 (±4)	350	341 (±4)[tl]	-	006 (±3)	243 (±2)
AN112B	42.123	110.937	C	s	068, 40 (±4)	350	pd	352 (±4)	018 (±3)	259 (±2)
AN-113	*41.823*	*110.837*	*A*	*c*	*200, 18 (±4)*	*~010*	*035 (±11)[k]*	*sf*	*sf*	*of*
AN-114	42.282	110.601	A	s, p	240, 15 (±3)	010	358 (±7)[tu]	sf	sf	286 (±3)
AN-115	42.545	110.617	H	s	268, 28 (±2)	360	349 (±7)[tu]	359 (±4)	sf	282 (±3)
AN-116	42.577	110.615	H	s	278, 10 (±3)	010	006 (±6)[tl]	-	of	249 (±2)
AN-117	42.508	110.617	H	s	081, 41 (±5)	347	350 (±7)[tu]	342 (±3)	017 (±9)	255 (±2)
AN-118	42.541	110.638	H	s	074, 45 (±5)	345	325 (±4)[tu]	340 (±4)	sf	277 (±3)
AN-119	*42.489*	*110.618*	*H*	*c*	*195, 39(±4)*	*~340*	*004 (±7)[tu]*	-	*352 (±3)*	*225 (±2)*
AN-120	42.439	110.628	A	s	230, 36 (±3)	335	349 (±11)[k]	-	347 (±5)	242 (±2)
AN-121	42.748	110.820	A	s	164, 12 (±1)	358	343 (±10)[k]	349 (±3)	344 (±3)	262 (±3)
AN-122	42.747	110.833	A	s	094, 43 (±3)	358	346 (±4)[tl]	-	358 (±2)	269 (±4)
An-123	42.725	110.902	A	s	263, 80 (±2)	355	340 (±7)[tl]	356 (±3)	354 (±3)	260 (±2)
AN-124	43.406	111.421	C	s	220, 46 (±4)	320	315 (±7)[tu]	-	322 (±5)	230 (±2)
AN-125	43.284	110.536	H	s	246, 43 (±4)	336	pd	-	323 (±5)	245 (±2)
AN-126	43.323	110.607	H	s	127, 09 (±3)	335	ha	-	337 (±7)	of
AN-127	43.305	110.608	H	s, r	144, 28 (±3)	335	ha	-	003 (±4)	-
AN-128	*43.345*	*110.586*	*H*	*c*	*223, 50 (±2)*	*335*	*351 (±5)[tl]*	-	*355 (±6)*	*254 (±4)*
AN-129	43.331	110.592	H	s	237, 37 (±4)	335	330 (±4)[tu]	-	333 (±7)	245 (±2)
AN-130	41.883	111.883	C	s, p	251, 36 (±4)	005	ha	-	016 (±3)	271 (±2)
AN-131	43.238	111.268	C	s	050, 58 (±5)	323	hs	327 (±3)	336 (±5)	244 (±3)
AN-132	43.236	111.269	C	s	241, 38 (±4)	323	325 (±5)[tl]	-	330 (±3)	235 (±2)
AN-133	43.338	111.312	C	s	249, 41 (±4)	328	345 (±5)[tu]	-	341 (±3)	252 (±3)
AN-134	43.411	111.436	C	s	236, 62 (±3)	317	323 (±7)[tu]	335 (±3)	329 (±3)	233 (±2)
AN-135	43.493	111.181	A	s, p	232, 66 (±3)	317	288 (±7)[tl]	-	296 (±2)	227 (±3)

Table 1. (continued)

Site	Lat	Long	Structure		Bedding	Trend	Paleomag[b]	Strain	AMS	LPS Dir
			Thrust	Setting						
AN-136	43.637	111.279	H	s	237, 40 (±2)	320	330 (±5)^{tu}	322 (±5)	328 (±2)	235 (±2)
AN-137	43.330	110.779	H	s, p	044, 52 (±2)	325	332 (±5)^{tl}	-	338 (±6)	235 (±2)
AN-138	42.863	110.834	A	s	251, 43 (±2)	345	345 (±7)^{tl}	-	358 (±5)	247 (±2)
AN-139	42.687	110.889	A	s	270, 70 (±2)	352	ha	002 (±3)	sf	255 (±3)
AN-140	42.889	111.237	M	s	218, 14 (±3)	315	ha		314 (±3)	232 (±2)
AN-141	43.433	111.036	A	s	232, 42 (±3)	319	325 (±7)^{k}	321 (±4)	294 (±5)	248 (±3)
AN-142	43.431	111.019	A	s	033, 61 (±3)	309	318 (±6)^{tu}	-	320 (±7)	214 (±2)
AN-143	*43.120*	*110.570*	*H*	*c*	*083, 102 (±3)*	*350*	*346 (±5)^{tl}*	*355 (±3)*	*350 (±4)*	*271 (±2)*
AN-144	43.122	110.548	H	s, p	046, 20 (±2)	350	ha	-	347 (±4)	264 (±2)
AN-145	42.976	110.695	H	s, p	274, 43 (±2)	353	ha	350 (±3)	331 (±8)	258 (±2)
AN-146	*42.493*	*110.745*	*A*	*c*	*279, 55 (±3)*	*~350*	*013 (±4)^{tu}*	-	*sf*	*262 (±3)*
AN-147	*42.519*	*110.719*	*A*	*c*	*243, 35 (±3)*	*~350*	*354 (±5)^{tu}*	-	*sf*	*253 (±2)*
AN-148	41.241	111.339	C	s, p	262, 34 (±2)	022	354 (±7)^{k}	-	041 (±6)	293 (±4)
AN-149	41.241	111.333	C	s, p	271, 29 (±2)	022	016 (±11)^{k}	-	035 (±2)	296 (±3)
AN-150	41.246	111.321	C	s, p	356, 24 (±3)	020	ha	-	of	292 (±2)
AN-151	42.095	111.245	C	s	097, 79 (±4)	005	ha	360 (±4)	358 (±4)	262 (±2)
AN-152	42.289	110.799	A	s	287, 35 (±2)	005	011 (±3)^{tl}	-	of	276 (±2)
AN-153	40.747	111.580	A	s, r	359, 70 (±5)	025	356 (±5)^{tl}	024 (±3)	019 (±3)	276 (±3)

[a]Site, site number and location given in Figure 6b. Lat, Long, latitude and longitude of site. Thrusts are C, Crawford system; A, Absaroka system; H, Hogsback system; M, Meade thrust, F, foreland; and settings are s, structurally simple; p, plunging fold; r, younger tilting; c, complex setting (overturned limb, oblique ramp or transfer zone); f, foreland; sites from complex settings and foreland are indicated by italics. Trend, structural trend estimated from geologic map data, approximate regional value given for oblique ramp/transfer zone area. Bedding, dip, dip direction of bedding (with α_{95} cone in parentheses); dip > 100 indicates overturned. Paleomag, restored paleomagnetic declinations (measurement uncertainty $\sigma_m \approx (0.4)\ \alpha_{95}/\cos(i)$ listed in parentheses), tl, lower Triassic; tu, upper Triassic component; k, Cretaceous component; pd, present-day viscous overprint; ha, $\alpha_{95} > 15°$; hs, high strain; ni, not interpretable. Strain, restored finite strain X directions estimated from reduction spots (measurement uncertainty $\sigma_m \approx (0.4)\ \alpha_{95}$ listed in parentheses), sf, dominant sedimentary fabric. AMS, restored K_{max} directions (measurement uncertainty $\sigma_m \approx (0.4)\ \alpha_{95}$ listed in parentheses), sf, dominant sedimentary fabric; of, oblique fabric; ni, not interpretable. LPS Dir, layer-parallel shortening direction based on restored pole to cleavage and high-angle fracture sets (measurement uncertainty $\sigma_m \approx (0.4)\ \alpha_{95}$ listed in parentheses); of, oblique fracture sets.

[b]Two declinations are listed for sites that preserve both Triassic and Cretaceous components.

[42] Least squares analysis of the 22 filtered K sites from all thrust systems gave a slope of 0.77 ± 0.26 (at 95%), determined for weighting factors related to measurement uncertainty, structural noise, and restoration uncertainty (70 to 100% unfolding) (Figure 10b). The larger confidence interval for the K component reflects fewer sites and larger site uncertainty mostly due to steeper inclination. Slopes for the Tr and K components are statistically indistinguishable, and so a strike test was done for pooled Tr and K component data, which yielded a slope of 0.76 ± 0.11. This indicates that the Wyoming salient was a progressive arc, with ~3/4 secondary curvature related to vertical axis rotation synchronous with large-scale thrusting and ~1/4 initial curvature.

3.4. Results for Finite Strain Analysis

[43] Finite strain was estimated at 44 sites, where adequate numbers of reduction spots were available for analysis, with 40 sites having well defined *X* (long) directions parallel to intersection of LPS fabrics and bedding, and 4 sites displaying dominantly oblate sedimentary fabrics (Table 1). Of the 40 sites with lineations, 34 were located in relatively simple structural settings. Strain ellipses along bedding planes, which record the ratio of LPS to tangential extension, display systematic variations around the salient (Figure 9b) [*Yonkee and Weil*, 2010]. *X* directions define a tangential pattern and corresponding tectonic shortening (*Z*) directions define a radial pattern at high angles to structural trend around the salient. Strain ellipses record from ~20% LPS in the Crawford system, to ~5% LPS in central parts of the Hogsback system.

[44] Least squares analysis of the 34 filtered *X* directions yielded a best fit slope of 0.89 ± 0.12 (Figure 10c). Residuals had an approximately normal distribution with a standard deviation of $s_r = 7°$ reflecting small measurement uncertainty and structural noise. Residuals were uncorrelated with structural trend and gave an acceptable goodness of fit. Although finite strain analysis provided well constrained fabric directions, reduction spots were not present at most sites, and thus AMS and mesoscopic structures were also used to analyze fabric directions.

3.5. Results for AMS Analysis

[45] The Ankareh Formation contained 99 sites with AMS ellipsoids having a definable magnetic lineation (K_{max}) at low angles to structural trend, 10 sites had lineations distinctly oblique to structural trend, 27 sites had a dominant oblate sedimentary fabric, and the remaining sites did not yield interpretable results (Table 1). Of the 99 sites with definable lineations, 85 were located in relatively simple structural settings. K_{max} directions, which are subparallel to the intersection of LPS fabrics with bedding, define a tangential pattern around the salient (Figure 9c) [*Weil and Yonkee*, 2009]. AMS fabric intensity (as measured by strength of the magnetic lineation) displays a similar pattern as strain intensity, with sedimentary fabrics widespread in the frontal Hogsback system, and moderate tectonic fabrics common in the western Crawford system. However, quan-

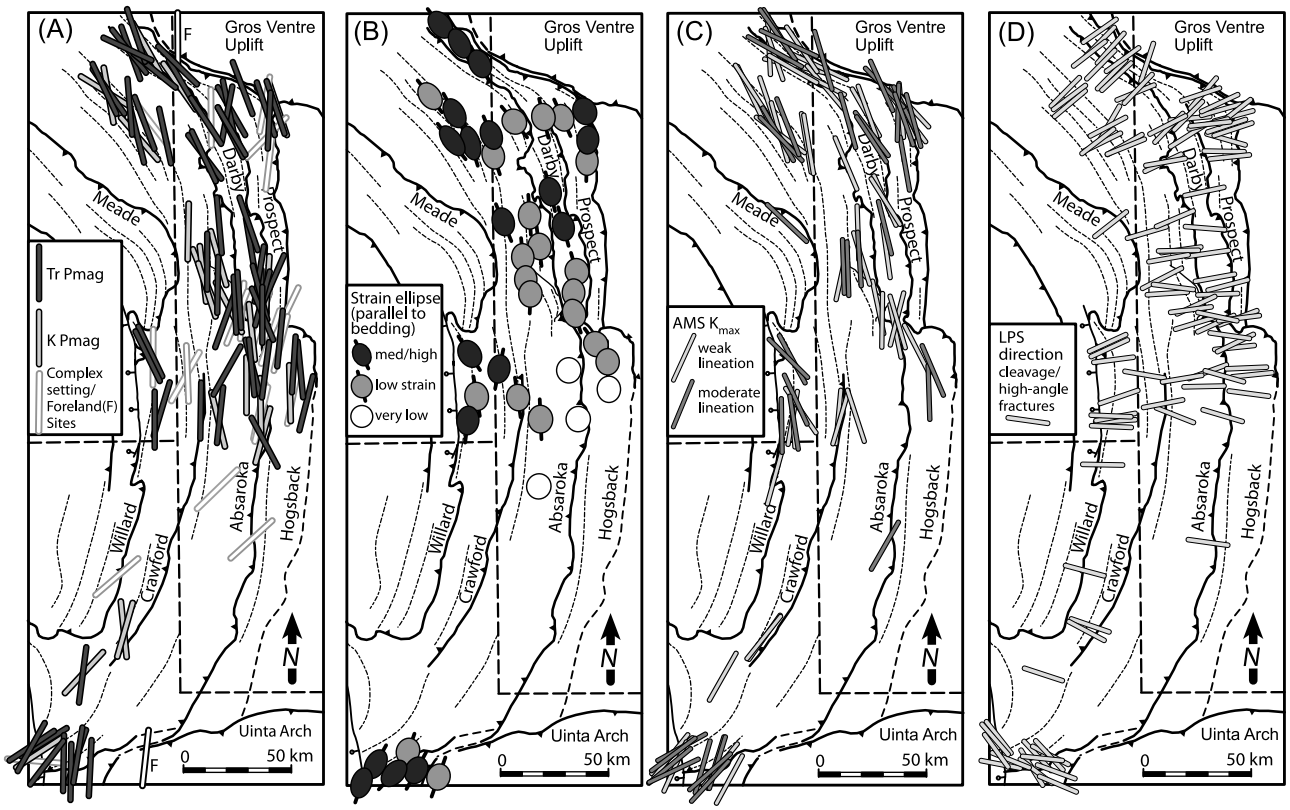

Figure 9. Maps showing restored directions for Ankareh Formation in the Wyoming salient. Major thrust systems (Crawford, Absaroka, Hogsback) are labeled. (a) Restored site-mean paleomagnetic declinations for prethrusting Triassic (Tr) component (black) and Cretaceous (K) remagnetization component (gray); declinations are plotted with respect to appropriate reference direction of 340° for Early Triassic and 350° for Late Triassic and Cretaceous components. Sites in northern and southern parts of the salient record counterclockwise and clockwise rotations, respectively. Modified from *Weil et al.* [2010]. (b) Bed-parallel strain ellipses estimated from reduction spots. Long (X) axes of ellipses define tangential pattern, and corresponding short (tectonic Z) axes define a radial pattern. Strain intensity increases westward and toward the salient ends. Modified from *Yonkee and Weil* [2010]. (c) AMS K_{max} directions, which are subparallel to intersection of LPS fabrics with bedding, define a tangential pattern. Intensity of magnetic lineation (shown by different gray shades) increases overall westward and toward salient ends but also varies with lithology. Modified from *Weil and Yonkee* [2009]. (d) LPS directions estimated from poles to cleavage and high-angle fracture sets define a radial pattern. Finite strain, AMS, and mesoscopic structures record similar patterns of LPS fabrics.

titative correlations between finite strain and AMS ellipsoid shape are complex and include effects of varying lithology.

[46] Least squares analysis of the 85 filtered K_{max} directions yielded a slope of 0.94 ± 0.09 (Figure 10d). Residuals had a quasi-normal distribution with a standard deviation of s_r = 15°, consistent with combined measurement uncertainty (σ_m ~ 3–10°), AMS "fabric variability" (σ_f ~ 10°; Figure 7d), and structural noise (σ_n ~ 8°). Including fabric variability, which reflects composite deformation and sedimentary fabrics, gave an acceptable goodness of fit (Q = 0.2), whereas not including variability gave an unacceptably poor goodness of fit (Q < 0.01). Although residuals are larger for AMS data, the confidence interval in slope is smaller than for finite strain, reflecting a greater number of sites where AMS was measured.

3.6. Results for Mesoscopic Structural Analysis

[47] LPS directions were estimated from cleavage and high-angle fracture sets at most sites, and define a radial pattern around the salient (Table 1 and Figure 9d) [*Yonkee and Weil*, 2010]. In detail, estimated LPS directions display minor (~10°) variations between sites in areas of similar trend, reflecting measurement uncertainty and structural noise.

[48] Of sites located in relatively simple structural settings, LPS directions were estimated from cleavage poles at 36 sites and from high-angle fracture sets at 69 sites; the other 20 sites either had oblique fractures or lacked measurable sets. A strike test of cleavage directions, which are most clearly related to early LPS, yielded a slope of 0.88 ± 0.10 (Figure 10e), statistically indistinguishable from the

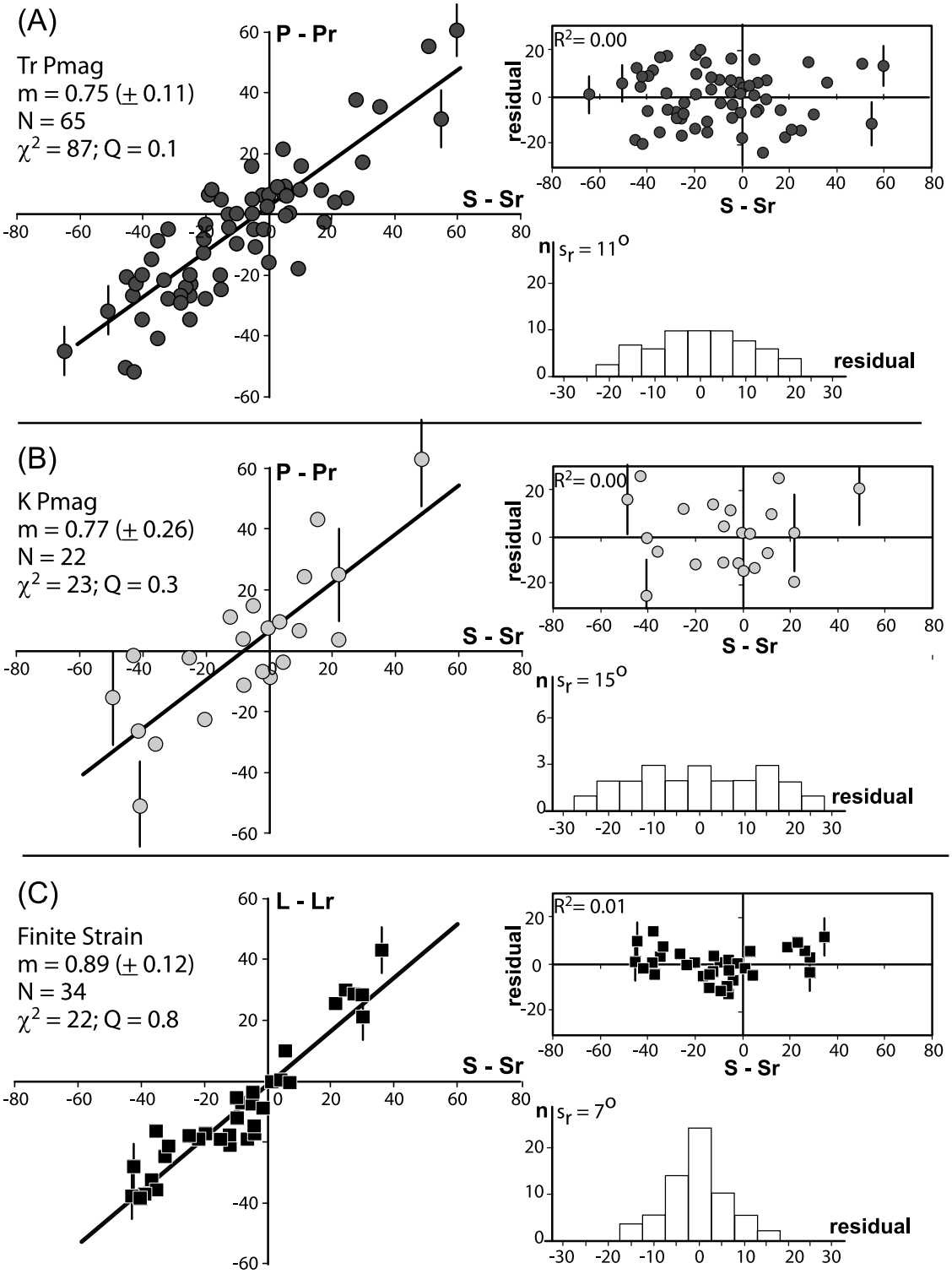
(A)
Tr Pmag
m = 0.75 (± 0.11)
N = 65
χ² = 87; Q = 0.1
P - Pr
S - Sr
R²= 0.00
residual
n
s_r = 11°
residual
(B)
K Pmag
m = 0.77 (± 0.26)
N = 22
χ² = 23; Q = 0.3
P - Pr
S - Sr
R²= 0.00
residual
n
s_r = 15°
residual
(C)
Finite Strain
m = 0.89 (± 0.12)
N = 34
χ² = 22; Q = 0.8
L - Lr
S - Sr
R²= 0.01
residual
n
s_r = 7°
residual

Figure 10

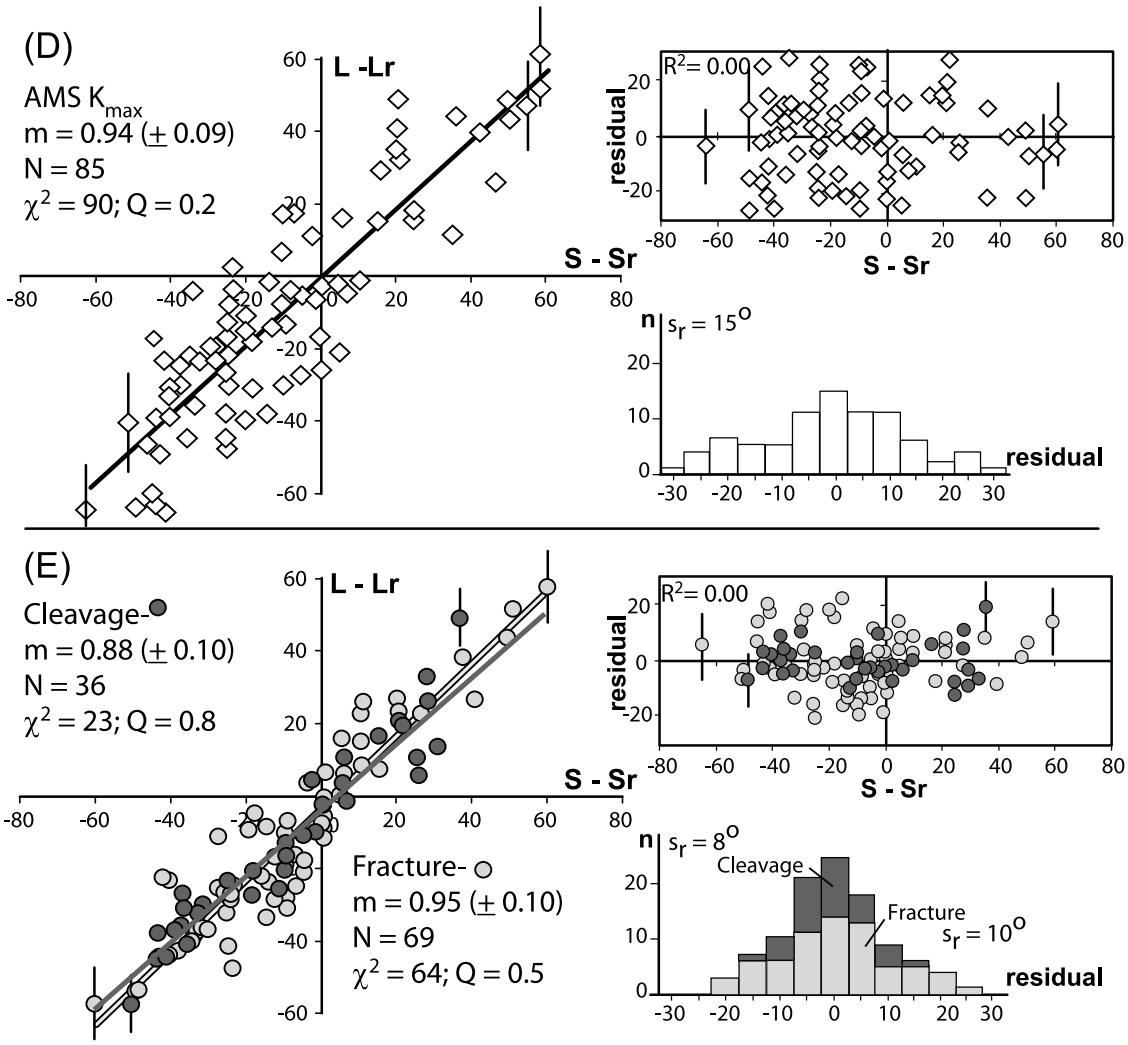

Figure 10. (continued)

Figure 10. (left) Strike tests for filtered data sets (excluding sites from overturned fold limbs, oblique ramps, and transfer zones) for Ankareh Formation in the Wyoming salient. Best fit slopes (m), 95% confidence intervals ($\pm 1.96\delta_m$, in parentheses), number of sites (N), total weighted misfit (χ^2), and goodness of fit (Q) listed. Example site $1\sigma_y$ uncertainty bars indicated. Structural trend relative to N-S (S-Sr) estimated from kilometer-scale geologic map relations. (right) Plots of residuals verses structural trend with square of correlation coefficient (R^2) and histograms of residuals with standard deviation (s_r). Data for plots complied from *Weil and Yonkee* [2009], *Weil et al.* [2010], and *Yonkee and Weil* [2010] (see Table 1 for data summary). (a) Paleomagnetic declinations for the Tr component relative to reference 340°/350° (P-Pr) define a slope of 0.75 (±0.11). (b) Paleomagnetic declinations for the K component relative to reference 350° define a slope of 0.77 (±0.26). The larger confidence interval mostly reflects steeper inclination and fewer sites. (c) Finite strain X directions relative to N-S (or orthogonal tectonic Z directions relative to E-W) estimated from reduction spots define a slope of 0.89 (±0.12). Residuals are small and have a normal distribution. Sites with a dominant sedimentary fabric not plotted. (d) AMS K_{max} directions relative to N-S define a slope of 0.94 (±0.09). Larger residuals for K_{max} directions are consistent with additional AMS fabric variability of 10°, which is included in site $1\sigma_y$ uncertainty error bars. Sites with a dominant sedimentary fabric not plotted. (e) LPS directions estimated from cleavage (dark gray circles) and high-angle fracture sets (light circles) define slopes of 0.88 (±0.10) and 0.95 (±0.10), respectively. Larger residuals for fractures are consistent with additional fracture fabric variability of 8°.

slope for finite strain. Residuals had an approximately normal distribution with a standard deviation of $s_r = 8°$, and gave an acceptable goodness of fit. A strike test of high-angle fractures, which mostly reflect partings along weak LPS fabrics, yielded a slope of 0.95 ± 0.10 (Figure 10e). Residuals had an approximately normal distribution with a larger standard deviation of $s_r = 10°$, consistent with additional fabric variability $\sigma_f \sim 8°$ that likely reflects fracturing during multiple deformation increments. Analysis of pooled cleavage and fracture orientations yielded a slope of 0.93 ± 0.10.

3.7. Comparison of Deformation Fabric and Paleomagnetic Data Sets

[49] Strike test slopes for finite strain data (m = 0.89 ± 0.12), AMS (m = 0.94 ± 0.09), cleavage (m = 0.88 ± 0.10), and high-angle fractures (m = 0.95 ± 0.10) are all close to 0.9, indicating AMS and mesoscopic structure orientations provide reasonable proxies for strain directions. Small differences between slopes partly reflect statistical uncertainty. Comparing deformation fabric slopes with the pooled paleomagnetic slope (m = 0.76±0.11), indicates that deformation fabrics started with a component of initial curvature, and thus cannot be directly used to estimate vertical axis rotation. For example, a site with final structural trend of −45°, relative paleomagnetic declination of −34° (for slope of 0.76), and final LPS direction of −41° relative to E–W (for slope of 0.9), would have experienced 34° counterclockwise rotation, giving an initial structural trend of −11° and initial LPS direction of −7°. Thus, simply using the final LPS direction and an assumed initial E–W direction, would overestimate rotation by 7°. However, accurate estimates of rotation from deformation fabrics are possible if initial orientations can be estimated by integrating paleomagnetic data. Incorporating 95% confidence intervals in paleomagnetic and deformation fabric data, the example site likely experienced 30–39° of rotation and had an initial LPS direction of −1–−13°. By applying a statistical approach with realistic site uncertainties, confidence intervals can be evaluated, confirming that the Wyoming salient is a progressive arc with components of secondary rotation and initial curvature of LPS fabrics.

3.8. Strike Tests for Individual Thrust Sheets

[50] To evaluate differences in the rotation patterns between thrust systems emplaced over different time intervals, strike tests for paleomagnetic data were completed for the Crawford, Absaroka, and Hogsback systems. Because Tr and K components gave statistically similar results, slopes were calculated for pooled Tr and K data in each thrust system. Pooled Tr and K (N = 15 + 8) sites in the Crawford system gave a slope of 0.80 ± 0.14 (Figure 11a). Within the Absaroka system, pooled Tr and K (N = 25 + 11) sites gave a slope of 0.74 ± 0.16 (Figure 11b), and within the Hogsback system, pooled Tr and K (N = 24 + 3) sites gave a slope of 0.65 ± 0.22 (Figure 11c). The slight decrease in slope from the middle Cretaceous Crawford system to the early Paleogene Hogsback system is statistically significant at a 90% level and may indicate a slightly greater proportion of secondary rotation in more internal, older thrust systems.

[51] Deformation fabric data were also analyzed separately for each thrust system. Because finite strain data, AMS, and mesoscopic structures gave similar results, slopes were calculated for pooled data sets for each thrust system. Analysis of pooled data yielded slopes of 0.93 ± 0.08 for the Crawford (Figure 11d), 0.98 ± 0.09 for the Absaroka (Figure 11e), and 0.93 ± 0.14 for the Hogsback system (Figure 11f). Consistent patterns between thrust systems indicate that LPS directions started subperpendicular to structural trend in all systems.

3.9. Comparison to Previous Rotation Estimates of the Wyoming Salient

[52] *Schwartz and Van der Voo* [1984] used a classic strike test to evaluate paleomagnetic data sets for parts of the Wyoming salient, and concluded that the northern Absaroka and Darby sheets experienced no systematic rotation, whereas significant rotation occurred in the northern Prospect sheet. In comparison, *McWhinnie et al.* [1990] interpreted no significant rotation in the northern Prospect sheet based on synthrusting remagnetization data, whereas data shown in Figure 11 indicate significant synthrusting rotation in all thrust systems. To understand these differences, we applied the weighted least squares method presented here to reexamine four previous data sets: (1) Triassic sites from the northern Prospect sheet [*Grubbs and Van der Voo*, 1976]; (2) Triassic sites from the northern Absaroka and Darby sheets [*Grubbs and Van der Voo*, 1976]; (3) remagnetized Jurassic Stump Formation sites from the northern Absaroka and Darby sheets [*Schwartz and Van der Voo*, 1984; *McWhinnie et al.*, 1990]; and (4) remagnetized Jurassic Twin Creek Formation sites from the northern Prospect sheet [*McWhinnie et al.*, 1990]. Strike tests were done using: (1) site strike values given by *Schwartz and Van der Voo* [1984] and *McWhinnie et al.* [1990] with uncertainty in structural trend of $\sigma_x \sim 10°$ and using equations (4) and (5) and (2) regional trend values estimated from geologic map patterns, filtering out sites from structurally complex areas, and using equations (1) and (2).

[53] Analysis of previous Triassic sites from the northern Prospect sheet (data set 1) using local site strikes yielded a slope of 1.49 ± 0.50 (at 95%) and large residuals with s_r = 20° (Figure 12a). However, one site (V) had a paleomagnetic $\alpha_{95} > 15°$ suggesting potential problems, and two sites (B and H) were located above a transfer zone in the Granite Creek thrust, resulting in locally anomalous patterns [*Weil et al.*, 2010]. Analysis of a filtered data set that excluded these three sites and used regional trend yielded a better defined slope of 0.80 ± 0.40, lower residuals with $s_r = 7°$, and improved goodness of fit. The slope for the filtered data set is statistically consistent with results presented in Figure 11c.

[54] Analysis of previous Triassic sites from the northern Absaroka and Darby sheets (data set 2) using local site strikes yielded a poorly defined slope of 0.48 ± 0.64 and large residuals with $s_r = 13°$ (Figure 12b). Analysis using regional trend values yielded a slope of 0.60 ± 0.62 and

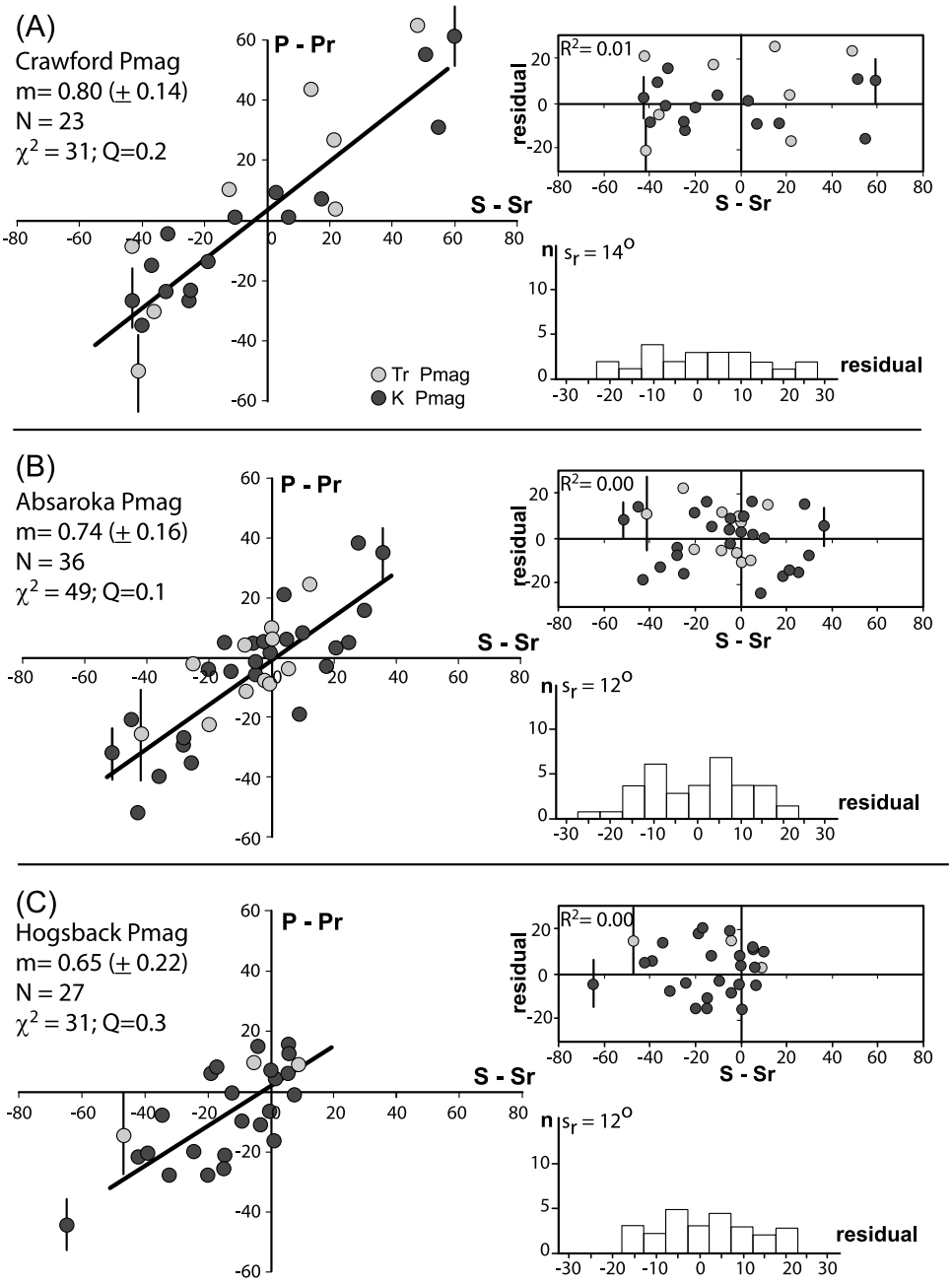

Figure 11. Strike tests for individual thrust systems (Crawford, Absaroka, Hogsback). Abbreviations same as in Figure 10. (a) Paleomagnetic declinations for pooled Tr (black) and K (gray) components relative to corresponding reference directions in the Crawford system define a slope of 0.80 (±0.14). (b) Paleomagnetic declinations for pooled Tr and K components in the Absaroka system define a slope of 0.74 (±0.16). (c) Paleomagnetic declinations for pooled Tr and K components in the Hogsback system define a slope of 0.65 (±0.22). The larger confidence interval reflects smaller variation in trend for sites. (d) Deformation fabric directions (black square, finite strain X; diamond, AMS K_{max}; dark gray and light gray circles, LPS estimated from cleavage and high-angle fracture sets) define a slope of 0.93 (±0.08) for the Crawford system. (e) Deformation fabric directions for the Absaroka system define a slope of 0.98 (±0.09). (f) Deformation fabric directions for the Hogsback system define a slope of 0.93 (±0.14). The larger confidence interval reflects smaller range in trend for sites in this system.

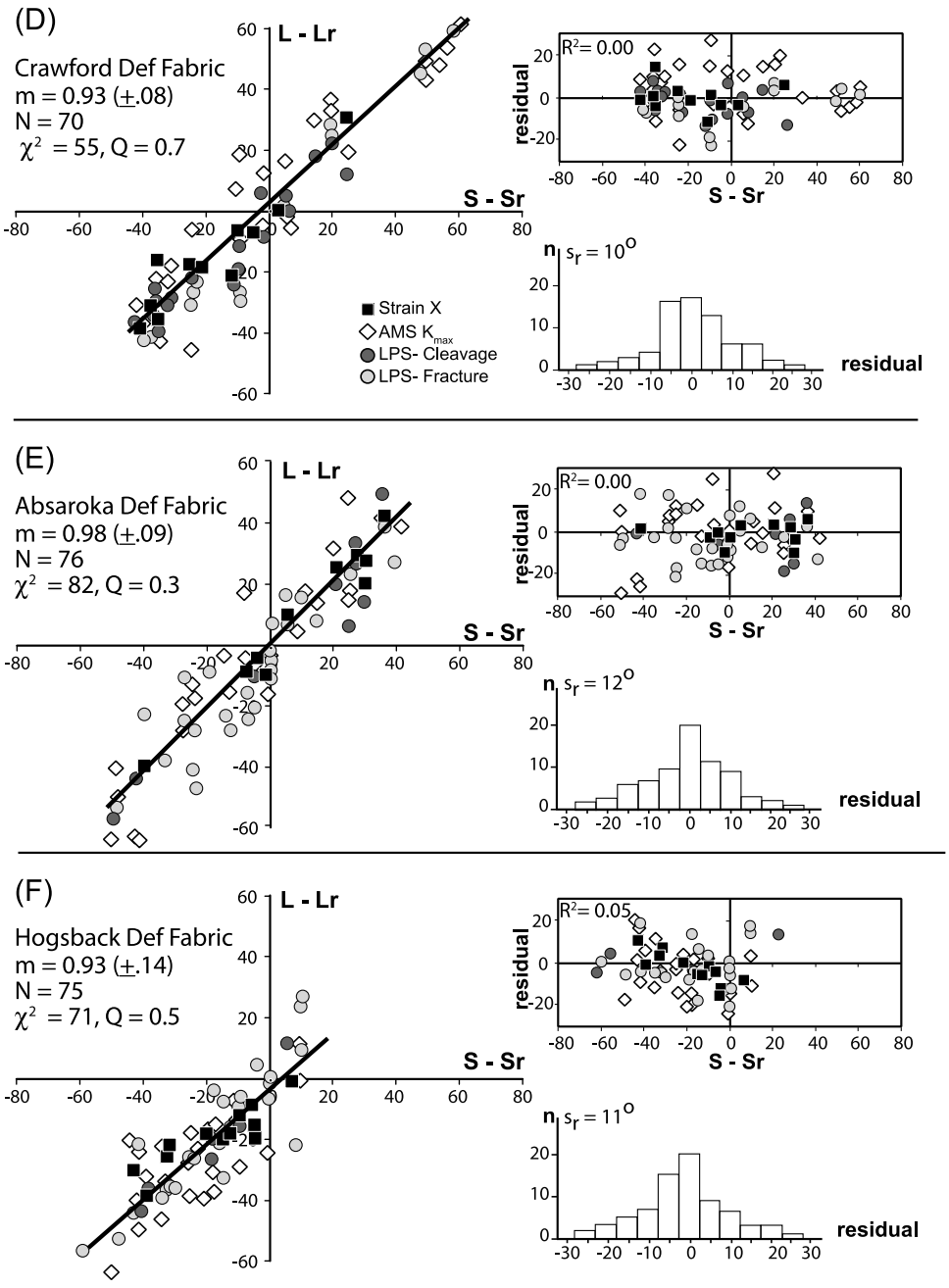

Figure 11. (continued)

smaller residuals. The large confidence interval (slope between 0.0 and 1.2) reflects limited trend distribution of sites. Although *Schwartz and Van der Voo* [1984] inferred no systematic rotation based on a low correlation coefficient, data are insufficient to interpret presence or absence of rotation. The larger data set for the Absaroka system shown in Figure 11b yielded a better defined slope of 0.74 ± 0.16, illustrating the importance of sampling over a wide range in structural trend.

[55] Interpretation of remagnetized Stump Formation sites in the northern Absaroka and Darby sheets (data set 3) is compounded by steeper paleomagnetic inclination ($i \approx 60°$) and uncertainty in timing of remagnetization. Using local site strikes and restored declinations for 80% unfolding given by *McWhinnie et al.* [1990, Table 2] yielded a poorly defined slope of 0.61 ± 0.70; using regional trend values yielded a slope of 1.07 ± 1.12 (Figure 12c). No significant interpretations of rotation can be made, reflecting steep paleomagnetic inclination and limited sampling.

[56] Interpretation of remagnetized Twin Creek Formation sites in the northern Prospect sheet (data set 4) is problematic due to structural complications. *McWhinnie et al.* [1990]

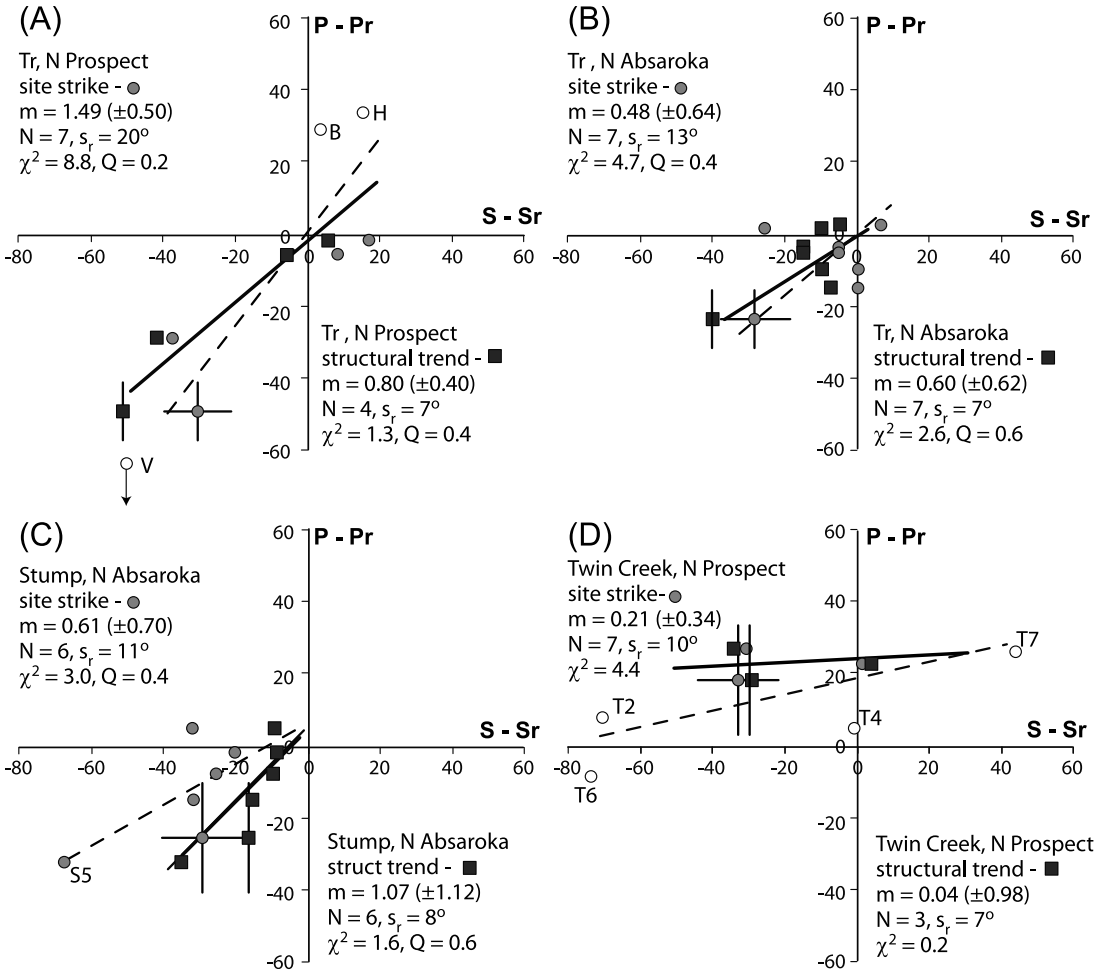

Figure 12. Strike tests for previously reported paleomagnetic data sets from the Wyoming salient. Abbreviations same as in Figure 10. Values in upper left are for unfiltered data sets calculated using local site strike (circles) with slope indicated by dashed line; values in lower right are for filtered data sets calculated using regional trend (squares) with slope indicated by solid line. Example site $1\sigma_y$ uncertainty error bars indicated. (a) Paleomagnetic data set for Triassic sites in the northern Prospect sheet reported by *Grubbs and Van der Voo* [1976]. Open circles labeled B and H are for sites in transfer zone and open circle labeled V has high paleomagnetic α_{95}; these sites are not included in the filtered data set. (b) Data set for Triassic sites in the northern Absaroka and Darby sheets reported by *Grubbs and Van der Voo* [1976]. Slopes have large confidence intervals due to limited range in trend. (c) Remagnetization data set for Stump Formation sites in the northern Absaroka and Darby sheets reported by *Schwartz and Van der Voo* [1984]. Circle labeled S5 comes from gentle limb of plunging a fold, which biases local site strike away from regional trend. Slopes are poorly defined due to steep inclination and limited range in trend. (d) Remagnetization data set for Twin Creek Formation sites in the northern Prospect sheet reported by *McWhinnie et al.* [1990]. Open circles labeled T6 and T7 have anomalous strikes related to cross folds and open circles labeled T2 and T4 are from overturned fold limbs; these sites are not included in the filtered data set. Slopes are poorly defined.

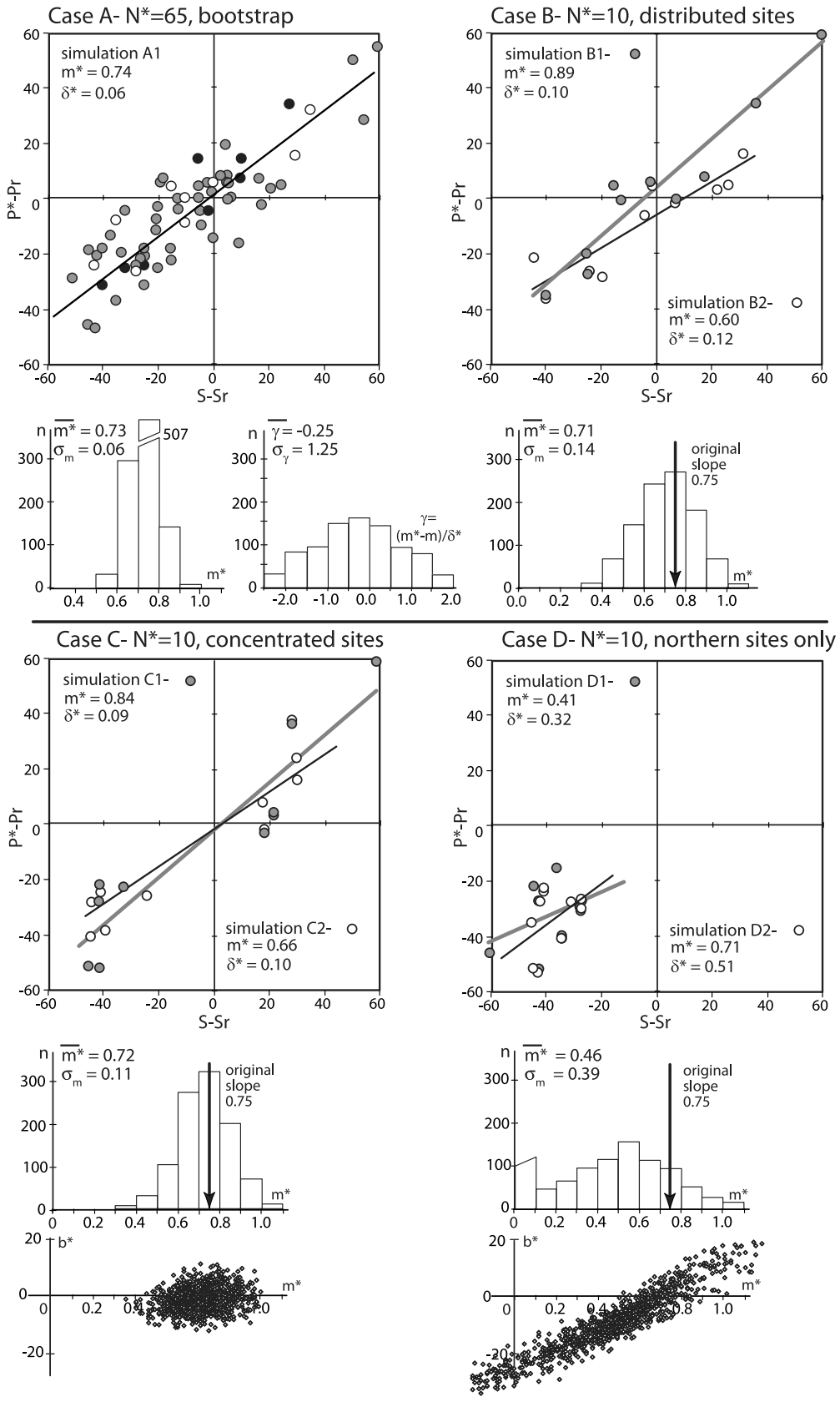
Case A- N*=65, bootstrap
simulation A1
m* = 0.74
δ* = 0.06
P*-Pr
S-Sr
n
m* = 0.73
σm = 0.06
507
m*
γ = -0.25
σγ = 1.25
γ=
(m*-m)/δ*
m* = 0.71
σm = 0.14
original
slope
0.75
Case B- N*=10, distributed sites
simulation B1-
m* = 0.89
δ* = 0.10
simulation B2-
m* = 0.60
δ* = 0.12
Case C- N*=10, concentrated sites
simulation C1-
m* = 0.84
δ* = 0.09
simulation C2-
m* = 0.66
δ* = 0.10
m* = 0.72
σm = 0.11
b*
Case D- N*=10, northern sites only
simulation D1-
m* = 0.41
δ* = 0.32
simulation D2-
m* = 0.71
δ* = 0.51
m* = 0.46
σm = 0.39

Figure 13

progressively restored paleomagnetic vectors by rotating about in situ bed strike and found maximum clustering at 80% untilting. However, some sites were from an area with cross folds and anomalous bed strikes, such that more complex restoration paths may be appropriate. Using simply restored declinations and local strike values reported by *McWhinnie et al.* [1990] yielded a slope of 0.21 ± 0.34 (Figure 12d). This estimate did not incorporate structural complexities, which cannot be adequately evaluated with available data. Excluding sites (T2, T4, T7) from cross-folded areas and overturned limbs, left only three filtered sites that yielded a very poorly constrained slope of 0.04 ± 0.98. Thus, no significant interpretations of rotation can be made.

4. Discussion

[57] Comparison of results from the case study with previous rotation estimates in the Wyoming salient illustrates the importance of systematic sampling and statistical analysis. To further investigate sampling design and test validity of the refined strike test method, the Tr component data set from the Wyoming salient was resampled for various number of sites (N*) and trend distributions (Figure 13). In a first simulation, bootstrap resampling (N* = 65) yielded individual resample slopes, m*, mostly between 0.6 and 0.8, with a mean of 0.73 and standard deviation of 0.06 (95% confidence interval ± 0.12) (Figure 13, case A), consistent with the estimated slope and confidence interval for the original data (Figure 10a). In detail, bootstrap slopes have slightly greater variance than expected, and some slopes are slightly biased toward lower values. These slight differences may reflect departure from ideal normal distribution of residuals. The relatively low value of model fit (Q = 0.1) for the Tr strike test is also suggestive of slight departure from ideal relations. Despite complications, however, the refined strike test gives consistent results, demonstrating applicability to geologic data sets.

[58] Large data sets may not always be obtainable due to limited exposures. To test the power of the method, simulations were run for various smaller data subsets. In a second simulation, 10 sites were randomly selected, with at least 3 sites each from the northern, central, and southern parts of the salient (N* = 10, $\Delta x \sim 90°$, distributed sites). Slopes of resamples ranged mostly from 0.4 to 1.1, with a mean of 0.71 and standard deviation of 0.14 (95% confidence interval ± 0.28) (Figure 13, case B). The larger deviation (which matches standard errors in individual slopes) reflects smaller sample size and is consistent with relations given by equation (8). In a third simulation, 5 sites were randomly selected each from the northern and southern parts of the salient (N* = 10, $\Delta x \sim 90°$, concentrated sites). Slopes of resamples ranged mostly from 0.5 to 1.0, with a mean of 0.73 and standard deviation of 0.12 (Figure 13, case C). Although this simulation yielded slightly smaller variance in slopes, concentrated sampling could miss along-strike variations in rotation patterns. In a fourth simulation, 10 sites were randomly selected from only the northern part of the salient (N* = 10, $\Delta x \sim 30°$). Slopes of resamples ranged widely from −0.4 to 1.2, with a lower, biased mean of 0.46 and a larger standard deviation of 0.39 (Figure 13, case D). Lower slopes are correlated with negative intercepts, with bias partly reflecting covariance in parameter estimates. Given a wide distribution of sites including salient ends, the least squares method provides reasonably accurate slopes with 95% confidence intervals of ~±0.3 to ~±0.1 for 10–60 sites (for a range in trend of 90°). The method breaks down for smaller sample sizes and limited trend distributions, where subtle complications in data may lead to bias and very large confidence intervals.

[59] The refined method developed here incorporates uncertainties in paleomagnetic and deformation fabric directions, which are needed to estimate weighting factors and evaluate goodness of model fit. Direction uncertainties in the Wyoming salient included intrasite measurement dispersion ($\sigma_m \sim 3$–10°), in addition to intersite structural noise ($\sigma_n \sim 8°$) from small-scale block rotations and stress/strain refraction, fabric variability ($\sigma_f \sim 8/10°$ for fracture/AMS data), and variable restoration paths ($\sigma_p < 5°$ for most sites). If direction uncertainties are unavailable, a strike test slope can still be estimated by setting all weighting factors to 1; however such an approach does not provide a measure of model fit. The refined method uses regional trend estimated from geologic map data. Although local bedding strike can be used, this introduces additional uncertainty and bias in areas with plunging folds and oblique structures.

Figure 13. Simulations for resampling Tr component data. Resampling done for cases A to D with different numbers of sites (N*) and distributions in structural trend. Examples of resampled data, slopes (m*), and standard errors (δ*) shown for each case, along with histogram of slopes for 1000 resamples with mean and standard deviation of m* listed. Case A, bootstrap (N* = 65) resampling of original data (gray, site resampled once; open, not resampled; black, resampled more than once). Histogram of resample slopes on left shows a mean close to the original Tr slope of 0.75 and a standard deviation (s_{m*}) similar to the standard error. Histogram of normalized residuals ($\gamma = [m* - m]/\delta*$) on right (with a theoretical mean of 0 and standard deviation of 1) is slightly skewed, indicating site data are likely not strictly normally distributed. Case B, small resample size (N* = 10) with distributed sites from north, central, and south domains. Slopes of resamples vary mostly between 0.4 and 1.0 and have larger standard errors related to smaller sample size. Case C, small resample size (N* = 10) with sites concentrated at salient ends (5 sites each from north and south domains). Slopes of resamples vary mostly between 0.5 and 0.9. Plot of resample slope (m*) verses intercept (b*) shows estimated parameters are uncorrelated. Case D, small resample size (N* = 10) with sites over limited range in trend (north domain only). Resample slopes vary widely between −0.4 and 1.0 with a mean biased to a lower value compared to the original slope. Plot of resample slope verses intercept shows correlation in estimated parameters.

[60] Strike test slopes provide critical constraints on angular correlations between paleomagnetic declinations, deformation fabric directions, and structural trend, but slopes must be combined with additional data to estimate spatial patterns of vertical axis rotation in a curved orogen. For example, two thrust systems may have the same paleomagnetic strike test slope, but display different distributions of curvature, with rotations more highly concentrated near the ends of a highly elliptical arc system compared to a circular arc system. Although paleomagnetic data provide a direct measure of rotation (or relative rotation if reference direction is unknown), suitable lithologies may only be exposed in limited areas. Deformation fabrics exposed over larger areas can then be used to estimate rotation patterns, if initial fabric curvature can be constrained by statistical relations to paleomagnetic data [e.g., *Weil et al.*, 2010]. By integrating paleomagnetic, deformation fabric, and structural trend data with a refined least squares method, spatial-temporal patterns of rotation can be evaluated, providing a powerful technique to understand origins of curved mountain systems.

5. Conclusions

5.1. General Use of the Weighted Least Squares Strike Test

[61] 1. Quantifying vertical axis rotation over a range of temporal and spatial scales is critical for understanding processes that produce curved mountain systems. The best way to quantify vertical axis rotation, and thus provide a key data set to test various kinematic models, is through paleomagnetic analysis done at appropriate scales. However, vertical axis rotation is just one component of the 3-D deformation field, and thus any viable kinematic model must also be consistent with structural and strain data.

[62] 2. Strike tests using a weighted least squares approach provide a powerful method to determine correlations between map-scale structural trend, rotations determined from paleomagnetic data, and changes in deformation fabric directions.

[63] 3. Systematic sampling with an adequate number and trend distribution of sites is critical for yielding well constrained strike test slopes.

[64] 4. Proper evaluation of total site uncertainty is important for estimating confidence intervals and evaluating goodness of model fit.

[65] 5. Failure to consider structural noise may result in inappropriately small confidence intervals, especially in areas with structural complications.

5.2. Case Study Results

[66] 1. Integrated paleomagnetic and structural analysis of the Wyoming salient has revealed systematic patterns of vertical axis rotation and deformation fabrics.

[67] 2. Paleomagnetic data indicate ~3/4 secondary rotation and 1/4 primary curvature in the Wyoming salient, with slightly greater relative rotation in the more interior Crawford system.

[68] 3. Finite strain, AMS, cleavage, and fracture directions all yield strike test slopes of ~0.9. Combined with paleomagnetic results, this indicates that early LPS fabrics had primary curvature and cannot be used alone to accurately estimate vertical axis rotations.

[69] 4. Integrating paleomagnetic, strain, AMS, and structural data allows consistencies and discrepancies between data sets to be evaluated, and provides a statistical means for evaluating use of deformation fabrics to estimate initial LPS directions and subsequent rotations.

[70] 5. Previous, varying interpretations of paleomagnetic data from different local studies in the Wyoming salient illustrate difficulties in estimating rotations from small data sets in areas with limited range in trend and structural complications.

[71] **Acknowledgments.** This work was supported by NSF grants EAR-0409103 and EAR-0408653. Insightful reviews by Mark Hudson and Randy Enkin significantly improved this paper.

References

Apotria, T. G. (1995), Thrust sheet rotation and out-of-plane strains associated with oblique ramps; an example from the Wyoming salient, U.S.A., *J. Struct. Geol.*, *17*, 647–662, doi:10.1016/0191-8141(94)00087-G.

Apotria, T. G., W. T. Snedden, J. H. Spang, and D. V. Wiltschko (1992), Kinematic models of deformation at an oblique ramp, in *Thrust Tectonics*, edited by K. R. McClay, pp. 141–154, Chapman and Hall, London.

Armstrong, F. C., and S. S. Oriel (1965), Tectonic development of the Idaho-Wyoming thrust belt, *AAPG Bull.*, *49*, 1847–1866.

Averbuch, O., D. Frizon de Lamotte, and C. Kissel (1992), Magnetic fabric as a structural indicator of the deformation path within a fold-thrust structure; a test case from the Corbières (NE Pyrenees, France), *J. Struct. Geol.*, *14*, 461–474, doi:10.1016/0191-8141(92)90106-7.

Bayona, G., W. A. Thomas, and R. Van der Voo (2003), Kinematics of thrust sheets within transverse zones; a structural and paleomagnetic investigation in the Appalachian thrust belt of Georgia and Alabama, *J. Struct. Geol.*, *25*, 1193–1212, doi:10.1016/S0191-8141(02)00162-1.

Burtner, R. L., and A. Nigrini (1994), Thermochronology of the Idaho-Wyoming thrust belt during the Sevier Orogeny: A new, calibrated, multiprocess thermal model, *AAPG Bull.*, *78*, 1586–1612.

Bevington, P. R. (1969), *Data Reduction and Error Analysis for the Physical Sciences*, McGraw-Hill, New York.

Blackstone, D. (1977), The overthrust belt salient of the Cordilleran fold belt- western Wyoming, southeastern Idaho, northeastern Utah, *Wyo. Geol. Assoc. Guidebook*, *29*, 367–384.

Borradaile, G. J. (1997), Deformation and paleomagnetism, *Surv. Geophys.*, *18*, 405–435, doi:10.1023/A:1006555906559.

Borradaile, G. J., and B. Henry (1997), Tectonic applications of magnetic susceptibility and its anisotropy, *Earth Sci. Rev.*, *42*, 49–93, doi:10.1016/S0012-8252(96)00044-X.

Borradaile, G. J., and D. H. Tarling (1981), The influence of deformation mechanisms on magnetic fabrics in weakly deformed rocks, *Tectonophysics*, *77*, 151–168, doi:10.1016/0040-1951(81)90165-7.

Borradaile, G. J., and D. H. Tarling (1984), Strain partitioning and magnetic fabrics in particulate flow, *Can. J. Earth Sci.*, *21*(6), 694–697, doi:10.1139/e84-075.

Cederquist, D. P., R. Van der Voo, and B. A. van der Pluijm (2006), Syn-folding remagnetization of Cambro-Ordovician carbonates from the Pennsylvania salient post-dates oroclinal rotation, *Tectonophysics*, *422*, 41–54, doi:10.1016/j.tecto.2006.05.005.

Channell, J. E. T., W. Lowrie, F. Medizza, and W. Alvarez (1978), Palaeomagnetism and tectonics in Umbria, Italy, *Earth Planet. Sci. Lett.*, *39*, 199–210, doi:10.1016/0012-821X(78)90196-6.

Constable, C., and L. Tauxe (1990), The bootstrap for magnetic susceptibility tensors, *J. Geophys. Res.*, *95*, 8383–8395, doi:10.1029/JB095iB06p08383.

Coogan, J. C. (1992), Structural evolution of piggyback basins in the Wyoming-Idaho-Utah thrust belt, *Mem. Geol. Soc. Am.*, *179*, 55–81.

Craddock, J. P., A. A. Kopania, and D. V. Wiltschko (1988), Interaction between the northern Idaho-Wyoming thrust belt and bounding basement blocks, central western Wyoming, in *Interaction of the Rocky Mountain Foreland and the Cordilleran Thrust Belt*, edited by C. J. Schmidt and W. J. Perry Jr., *Mem. Geol. Soc. Am.*, *171*, 333–351.

Crosby, G. W. (1969), Radial movements in the western Wyoming salient of the Cordilleran overthrust belt, *Geol. Soc. Am. Bull.*, *80*, 1061–1077, doi:10.1130/0016-7606(1969)80[1061:RMITWW]2.0.CO;2.

DeCelles, P. G. (1994), Late Cretaceous- Paleocene synorogenic sedimentation and kinematic history of the Sevier thrust belt, northeast Utah and southwest Wyoming, *Geol. Soc. Am. Bull.*, *106*, 32–56, doi:10.1130/0016-7606(1994)106<0032:LCPSSA>2.3.CO;2.

DeCelles, P. G. (2004), Late Jurassic to Eocene evolution of the Cordilleran thrust belt and foreland basin system, western U.S.A., *Am. J. Sci.*, *304*, 105–168, doi:10.2475/ajs.304.2.105.

Demarest, H. N., Jr. (1983), Error analysis for the determination of tectonic rotation from paleomagnetic data, *J. Geophys. Res.*, *88*, 4321–4328, doi:10.1029/JB088iB05p04321.

Dixon, J. S. (1982), Regional structural synthesis, Wyoming salient of the western overthrust belt, *AAPG Bull.*, *10*, 1560–1580.

Eldredge, S., and R. Van der Voo (1988), Paleomagnetic study of thrust sheet rotations in the Helena and Wyoming salients of the northern Rocky Mountains, in *Interaction of the Rocky Mountain Foreland and the Cordilleran Thrust Belt*, edited by C. J. Schmidt and W. J. Perry Jr., *Mem. Geol. Soc. Am.*, *171*, 319–332.

Eldredge, S., V. Bachtadse, and R. Van der Voo (1985), Paleomagnetism and the orocline hypothesis, *Tectonophysics*, *119*, 153–179, doi:10.1016/0040-1951(85)90037-X.

Ferrill, D. A., and R. H. Groshong (1993), Kinematic model for the curvature of the northern Subalpine Chain, France, *J. Struct. Geol.*, *15*, 523–541, doi:10.1016/0191-8141(93)90146-2.

Fisher, R. A. (1953), Dispersion on a sphere, *Proc. R. Soc. London, Ser. A*, *217*, 295–305, doi:10.1098/rspa.1953.0064.

Geiser, P. A., and T. Engelder (1983), The distribution of layer parallel shortening fabrics in the Appalachian foreland of New York and Pennsylvania: Evidence for two non-coaxial phases of the Alleghanian orogeny, in *Contributions to the Tectonics and Geophysics of Mountain Chains*, edited by R.D. Hatcher Jr. et al., *Mem. Geol. Soc. Am.*, *158*, 161–175.

Gray, M. B., and J. Stamatakos (1997), New model for evolution of fold and thrust belt curvature, based on integrated structural and paleomagnetic results from the Pennsylvania salient, *Geology*, *25*, 1067–1070, doi:10.1130/0091-7613(1997)025<1067:NMFEOF>2.3.CO;2.

Grubbs, K. L., and R. Van der Voo (1976), Structural deformation of the Idaho-Wyoming overthrust belt (USA), as determined by Triassic paleomagnetism, *Tectonophysics*, *33*, 321–336, doi:10.1016/0040-1951(76)90151-7.

Hext, G. R. (1963), The estimation of second-order tensors, with related tests and designs, *Biometrika*, *50*, 353–373.

High, L. R., and M. D. Picard (1969), Stratigraphic relations within upper Chugwater group (Triassic), Wyoming, *AAPG Bull.*, *53*, 1091–1104.

Hindle, H., and M. Burkhard (1999), Strain, displacement and rotation associated with the formation of curvature on fold belts; the example of the Jura arc, *J. Struct. Geol.*, *21*, 1089–1101, doi:10.1016/S0191-8141(99)00021-8.

Hirt, A. M., and W. Lowrie (1988), Paleomagnetism of the Umbria-Arches orogenic belt, *Tectonophysics*, *146*, 91–106, doi:10.1016/0040-1951(88)90084-4.

Hirt, A. M., W. Lowrie, M. Julivert, and M. L. Arboleya (1992), Paleomagnetic results in support of a model for the origin of the Asturian arc, *Tectonophysics*, *213*, 321–339, doi:10.1016/0040-1951(92)90461-E.

Hogan, J. P., and W. M. Dunne (2001), Calculation of shortening due to outcrop-scale deformation and its relation to regional deformation patterns, *J. Struct. Geol.*, *23*, 1507–1529, doi:10.1016/S0191-8141(01)00016-5.

Irving, E., and N. D. Opdyke (1965), The paleomagnetism of the Bloomsburg redbeds and its possible application to the tectonic history of the Appalachians, *Geophys. J. R. Astron. Soc.*, *9*, 153–167.

Kent, D. (1988), Further paleomagnetic evidence for oroclinal rotation in the central folded Appalachians from the Bloomsburg and the Mauch Chunk formations, *Tectonics*, *7*, 749–759, doi:10.1029/TC007i004p00749.

Kent, D., and N. D. Opdyke (1985), Multicomponent magnetization from the Mississippian Mauch Chunk Formation of the central Appalachians and their tectonic implications, *J. Geophys. Res.*, *90*, 5371–5383, doi:10.1029/JB090iB07p05371.

Kent, J. T. (1982), The Fisher-Bingham distribution on the sphere, *J. R. Stat. Soc., Ser. B*, *44*, 71–80.

Kissel, C., E. Barrier, C. Laj, and T. Q. Lee (1986), Magnetic fabric in "undeformed" marine clays from compressional zones, *Tectonics*, *5*, 769–781, doi:10.1029/TC005i005p00769.

Kodama, K. P. (1988), Remanence rotation due to rock strain during folding and the stepwise application of the fold test, *J. Geophys. Res.*, *93*, 3357–3371, doi:10.1029/JB093iB04p03357.

Kotasek, J., and M. Krs (1965), Palaeomagnetic study of tectonic rotation in the Carpathian mountains of Czechoslovakia, *Palaeogeogr. Palaeoclimatol. Palaeoecol.*, *1*, 39–49, doi:10.1016/0031-0182(65)90005-2.

Kummel, B. (1954), Triassic stratigraphy of southeastern Idaho and adjacent areas [Wyoming-Montana], *U. S. Geol. Surv. Prof. Pap.*, *P0254-H*, 165–194.

Lickorish, W. H., M. Ford, J. Burgisser, and P. R. Cobbold (2002), Arcuate thrust systems in sandbox experiments: A comparison to the external arcs of the Western Alps, *Geol. Soc. Am. Bull.*, *114*, 1089–1107.

Lowrie, W., and A. M. Hirt (1986), Paleomagnetism in arcuate mountain belts, in *The Origin of Arcs*, *Dev. Geotectonics 21*, pp. 141–158, Elsevier, Amsterdam.

MacDonald, W. D. (1980), Net tectonic rotation, apparent tectonic rotation and structural tilt correction in paleomagnetic studies, *J. Geophys. Res.*, *85*, 3659–3669, doi:10.1029/JB085iB07p03659.

Marshak, S. (2004), Salients, recesses, arcs, oroclines, and syntaxes; a review of ideas concerning the formation of map-view curves in fold-thrust belts, in *Thrust Tectonics and Hydrocarbon Systems*, edited by K. R. McClay, *AAPG Mem.*, *82*, 131–156.

McFadden, P. L., and A. B. Reid (1982), Analysis of paleomagnetic inclination data, *Geophys. J. R. Astron. Soc.*, *69*, 307–319.

McFadden, P. L., R. T. Merrill, M. W. McElhinny, and S. Lee (1991), Reversals of the Earth's magnetic fields and temporal variations of the dynamo families, *J. Geophys. Res.*, *96*, 3923–3933, doi:10.1029/90JB02275.

McNaught, M. (1994), Modifying the normalized Fry method for aggregates of non-elliptical grains, *J. Struct. Geol.*, *16*, 493–503, doi:10.1016/0191-8141(94)90093-0.

McWhinnie, S. T., B. A. van de Pluijm, and R. Van der Voo (1990), Remagnetizations and thrusting in the Idaho-Wyoming overthrust belt, *J. Geophys. Res.*, *95*, 4551–4559, doi:10.1029/JB095iB04p04551.

Miller, J. D., and D. V. Kent (1986a), Synfolding and prefolding magnetizations in the Upper Devonian Catskill Formation of eastern Pennsylvania: Implications for the tectonic history of Acadia, *J. Geophys. Res.*, *91*, 12,791–12,803, doi:10.1029/JB091iB12p12791.

Miller, J. D., and D. V. Kent (1986b), Paleomagnetism of the Upper Devonian Catskill Formation from the southern limb of the Pennsylvania Salient: Possible evidence of oroclinal rotation, *Geophys. Res. Lett.*, *13*, 1173–1176, doi:10.1029/GL013i011p01173.

Mitra, G. (1994), Strain variation in thrust sheets across the Sevier fold-and-thrust belt (Idaho-Utah-Wyoming): Implications for section restoration and wedge taper evolution, *J. Struct. Geol.*, *16*, 585–602, doi:10.1016/0191-8141(94)90099-X.

Mitra, G., and W. A. Yonkee (1985), Spaced cleavage and its relationship to folds and thrusts in the Idaho-Utah-Wyoming thrust belt of the Rocky Mountain Cordilleras, *J. Struct. Geol.*, *7*, 361–373, doi:10.1016/0191-8141(85)90041-0.

Mulchrone, K. F., F. O'Sullivan, and P. A. Meere (2003), Finite strain estimation using the mean radial length of elliptical objects with bootstrap confidence intervals, *J. Struct. Geol.*, *25*, 529–539, doi:10.1016/S0191-8141(02)00049-4.

Muttoni, G., A. Argnani, D. V. Kent, N. Abrahamsen, and U. Cibin (1998), Paleomagnetic evidence for Neogene tectonic rotations in the northern Apennines, Italy, *Earth Planet. Sci. Lett.*, *154*, 25–40, doi:10.1016/S0012-821X(97)00183-0.

Muttoni, G., L. Lanci, A. Argnani, A. M. Hirt, U. Cibin, N. Abrahamsen, and W. Lowrie (2000), Paleomagnetic evidence for a Neogene two-phase counterclockwise tectonic rotation in the northern Apennines (Italy), *Tectonophysics*, *326*, 241–253, doi:10.1016/S0040-1951(00)00140-2.

Ong, P. F., B. A. van der Pluijm, and R. Van der Voo (2007), Early rotation and late folding in the Pennsylvania Salient (U.S. Appalachians): Evidence from calcite-twinning analysis of Paleozoic carbonates, *Geol. Soc. Am. Bull.*, *119*, 796–804, doi:10.1130/B26013.1.

Parés, J. M., and J. Dinarès Turell (1993), Magnetic fabric in two sedimentary rock-types from the southern Pyrenees, *J. Geomagn. Geoelectr.*, *45*, 193–205.

Parés, J. M., R. Van der Voo, J. A. Stamatakos, and A. Pérez-Estaún (1994), Remagnetization and postfolding oroclinal rotations in the Cantabrian/Asturian arc, northern Spain, *Tectonics*, *13*, 1461–1471, doi:10.1029/94TC01871.

Parés, J. M., B. A. van der Pluijm, and J. Dinares-Turell (1999), Evolution of magnetic fabrics during incipient deformation of mudrocks (Pyrenees, northern Spain), *Tectonophysics*, *307*, 1–14, doi:10.1016/S0040-1951(99)00115-8.

Paterson, S. R., H. Yu, and G. Oertel (1995), Primary and tectonic fabric intensities in mudrocks, *Tectonophysics*, *247*, 105–119, doi:10.1016/0040-1951(94)00199-J.

Perroud, H. (1986), Paleomagnetic evidence for tectonic rotations in the Variscan Mountain Belt, *Tectonics*, *5*, 205–214, doi:10.1029/TC005i002p00205.

Pueyo, E. L., J. M. Parés, H. Millan, and A. Pocovi (2003), Conical folds and apparent rotations in paleomagnetism (a case study in the southern Pyrenees), *Tectonophysics*, *362*, 345–366, doi:10.1016/S0040-1951(02)00645-5.

Ries, A. C., and R. M. Shackleton (1976), Patterns of strain variation in arcuate fold belts, *Proc. R. Soc. London, Ser. A*, *283*, 281–288.

Rochette, P., M. Jackson, and C. Aubourg (1992), Rock magnetism and the interpretation of anisotropy of magnetic susceptibility, *Rev. Geophys.*, *30*, 209–226, doi:10.1029/92RG00733.

Royse, F. (1993), An overview of the geologic structure of the thrust belt in Wyoming, northern Utah, and eastern Idaho, in *Geology of Wyoming*, edited by A. W. Snoke, J. R. Steidtmann, and S. M. Roberts, *Memoir 5*, pp. 272–311, Wyo. State Geol. Surv., Laramie.

Royse, F., M. A. Warner, and D. L. Reese (1975), Thrust belt structural geometry and related stratigraphic problems, Wyoming-Idaho-northern Utah, in *Deep Drilling Frontiers of the Central Rocky Mountains*, edited by D. W. Bolyard, pp. 41–54, Rocky Mt. Assoc. of Geol., Denver.

Rubey, W. W. (1973), Geologic map of the Afton quadrangle and part of the Big Piney quadrangle, Lincoln and Sublette counties, Wyoming, *U.S. Geol. Surv. Map I-686*, scale 1:62,500.

Sagnotti, L., and F. Speranza (1993), Magnetic fabric analysis of the Plio-Pleistocene clayey units of the Sant'Arcangelo Basin, southern Italy, *Phys. Earth Planet. Inter.*, *77*, 165–176, doi:10.1016/0031-9201(93)90096-R.

Schwartz, S. Y., and R. Van der Voo (1983), Paleomagnetic evaluation of the orocline hypothesis in the central and southern Appalachians, *Geophys. Res. Lett.*, *10*, 505–508, doi:10.1029/GL010i007p00505.

Schwartz, S. Y., and R. Van der Voo (1984), Paleomagnetic study of thrust sheet rotation during foreland impingement in the Wyoming-Idaho overthrust belt, *J. Geophys. Res.*, *89*, 10,071–10,086, doi:10.1029/JB089iB12p10077.

Shimamoto, T., and Y. Ikeda (1976), A simple algebraic method for strain estimation from deformed ellipsoidal objects; 1, Basic theory, *Tectonophysics*, *36*, 315–337, doi:10.1016/0040-1951(76)90107-4.

Stamatakos, J. A., and A. M. Hirt (1994), Paleomagnetic considerations of the development of the Pennsylvania salient in the central Appalachians, *Tectonophysics*, *231*, 237–255, doi:10.1016/0040-1951(94)90037-X.

Stamatakos, J. A., and K. P. Kodama (1991a), The effects of grain-scale deformation on the Bloomsburg Formation pole, *J. Geophys. Res.*, *96*, 17,919–17,933, doi:10.1029/91JB01499.

Stamatakos, J. A., and K. P. Kodama (1991b), Flexural flow folding and the paleomagnetic fold test: An example of strain reorientation of remanence in the Mauch Chunk Formation, *Tectonics*, *10*, 807–819, doi:10.1029/91TC00366.

Stewart, S. A. (1995), Paleomagnetic analysis of fold kinematics and implications for geological models of the Cantabrian/Asturian Arc, north Spain, *J. Geophys. Res.*, *100*, 20,079–20,094, doi:10.1029/95JB01482.

Sussman, A. J., and A. B. Weil (2004), Orogenic curvature: Integrating paleomagnetic and structural analysis, *Spec. Pap. Geol. Soc. Am.*, *383*, 1–271.

Tauxe, L. (1998), *Paleomagnetic Principles and Practice*, *Mod. Approach. Geophys.*, vol. 17, 299 pp., Kluwer Acad., London.

Torsvik, T., J. C. Briden, and M. A. Smethurst (1999), SuperIAPD99—Software package, Geol. Surv. Norway, Trondheim.

van der Pluijm, B. A. (1987), Grain-scale deformation and the fold test; evaluation of syn-folding remagnetization, *Geophys. Res. Lett.*, *14*, 155–157, doi:10.1029/GL014i002p00155.

Van der Voo, R. (2004), Paleomagnetism, oroclines, and growth of the continental crust, *GSA Today*, *14*, 4–9, doi:10.1130/1052-5173(2004)014<4:POAGOT>2.0.CO;2.

Van der Voo, R., and J. E. T. Channell (1980), Paleomagnetism in orogenic belts, *Rev. Geophys. Space Phys.*, *18*, 455–481, doi:10.1029/RG018i002p00455.

Van der Voo, R., J. A. Stamatakos, and J. M. Parés (1997), Kinematic constraints on thrust-belt curvature from syndeformational magnetizations in the Lagos del Valle syncline in the Cantabrian Arc, Spain, *J. Geophys. Res.*, *102*, 10,105–10,120, doi:10.1029/97JB00263.

Weil, A. B. (2006), Kinematics of orocline tightening in the core of an arc: Paleomagnetic analysis of the Ponga Unit, Cantabrian Arc, northern Spain, *Tectonics*, *25*, TC3012, doi:10.1029/2005TC001861.

Weil, A. B., and A. Sussman (2004), Classification of curved orogens based on the timing relationships between structural development and vertical-axis rotations, in *Paleomagnetic and Structural Analysis of Orogenic Curvature*, edited by A. J. Sussman and A. B. Weil, *Spec. Pap. Geol. Soc. Am.*, 383, 1–17.

Weil, A. B., and R. Van der Voo (2002), The evolution of the paleomagnetic fold test as applied to complex geologic situations, illustrated by a case study from northern Spain, *Phys. Chem. Earth*, *27*, 1223–1235.

Weil, A. B., and W. A. Yonkee (2009), Anisotropy of magnetic susceptibility in weakly deformed redbeds from the Wyoming salient, Sevier thrust belt: Relations to layer-parallel shortening and orogenic curvature, *Lithosphere*, *1*, 235–256, doi:10.1130/L42.1.

Weil, A. B., R. Van der Voo, B. A. van der Pluijm, and J. M. Parés (2000), Unraveling the timing and geometric characteristics of the Cantabria-Asturias Arc (northern Spain) through paleomagnetic analysis, *J. Struct. Geol.*, *22*, 735–756, doi:10.1016/S0191-8141(99)00188-1.

Weil, A. B., R. Van der Voo, and B. A. van der Pluijm (2001), New paleomagnetic data from the southern Cantabria-Asturias Arc, northern Spain: Implications for true oroclinal rotation and the final amalgamation of Pangea, *Geology*, *29*, 991–994, doi:10.1130/0091-7613(2001)029<0991:OBAEAT>2.0.CO;2.

Weil, A. B., W. A. Yonkee, and A. J. Sussman (2010), Reconstructing the kinematic evolution of curved mountain belts: A paleomagnetic study of Triassic red beds from the Wyoming salient, Sevier thrust belt, U.S.A., *Geol. Soc. Am. Bull.*, *122*, 3–23, doi:10.1130/B26483.1.

Wilkerson, M. S., T. Apotria, and T. Farid (2002), Interpreting the geologic map expression of contractional fault-related fold terminations: Lateral/oblique ramps versus displacement gradients, *J. Struct. Geol.*, *24*, 593–607, doi:10.1016/S0191-8141(01)00111-0.

Wiltschko, D. V., and J. A. Dorr (1983), Timing of deformation in overthrust belt and foreland of Idaho, Wyoming and Utah, *AAPG Bull.*, *67*, 1304–1322.

Woodward, N. B. (1986), Thrust geometry of the Snake River Range, Idaho and Wyoming, *Geol. Soc. Am. Bull.*, *97*, 178–193, doi:10.1130/0016-7606(1986)97<178:TFGOTS>2.0.CO;2.

Yonkee, W. A. (2005), Strain patterns within part of the Willard thrust sheet, Idaho-Utah-Wyoming thrust belt, *J. Struct. Geol.*, *27*, 1315–1343, doi:10.1016/j.jsg.2004.06.014.

Yonkee, W. A., and A. B. Weil (2010), Reconstructing the kinematic evolution of curved mountain belts: Internal strain patterns in the Wyoming salient, Sevier thrust belt, U.S.A., *Geol. Soc. Am. Bull.*, *122*, 24–49, doi:10.1130/B26484.1.

York, D. (1968), Least-squares fitting of a straight line with correlated errors, *Earth Planet. Sci. Lett.*, *5*, 320–324, doi:10.1016/S0012-821X(68)80059-7.

Zijderveld, J. D. A. (1967), AC demagnetization of rocks: Analysis of results, in *Methods in Paleomagnetism*, edited by D. W. Collison, S. K. Runcorn, and K. M. Creer, pp. 254–286, Elsevier, New York.

A. B. Weil, Department of Geology, Bryn Mawr College, Bryn Mawr, PA 19010, USA.

A. Yonkee, Department of Geosciences, Weber State University, Ogden, UT 84408, USA. (ayonkee@weber.edu)